FRONTIERS OF PHYSICS

TOPICAL REVIEW
Volume 18 / Issue 3 / 33601 / 2023

The rise of two-dimensional tellurium for next-generation electronics and optoelectronics

Tao Zhu[1,2], Yao Zhang[1,2], Xin Wei[2], Man Jiang[1,†], Hua Xu[2,‡]

1 State Key Laboratory of Photon-Technology in Western China Energy, International Collaborative Center on Photoelectric Technology and Nano Functional Materials, Institute of Photonics & Photon Technology, School of Physics, Northwest University, Xi'an 710069, China

2 Key Laboratory of Applied Surface and Colloid Chemistry of Ministry of Education, Shaanxi Key Laboratory for Advanced Energy Devices, School of Materials Science and Engineering, Shaanxi Normal University, Xi'an 710119, China

Corresponding authors. E-mail: †jmnwu@nwu.edu.cn, ‡xuhua-nano@snnu.edu.cn

Received November 5, 2022; accepted November 25, 2022

ABSTRACT

Single-element two-dimensional (2D) tellurium (Te) which possesses an unusual quasi-one-dimensional atomic chain structure is a new member in 2D materials family. 2D Te possesses high carrier mobility, wide tunable bandgap, strong light-matter interaction, better environmental stability, and strong anisotropy, making Te exhibit tremendous application potential in next-generation electronic and optoelectronic devices. However, as an emerging 2D material, the research on fundamental property and device application of Te is still in its infancy. Hence, this review summarizes the most recent research progresses about the new star 2D Te and discusses its future development direction. Firstly, the structural features, basic physical properties, and various preparation methods of 2D Te are systemically introduced. Then, we emphatically summarize the booming development of 2D Te-based electronic and optoelectronic devices including field effect transistors, photodetectors and van der Waals heterostructure photodiodes. Finally, the future challenges, opportunities, and development directions of 2D Te-based electronic and optoelectronic devices are prospected.

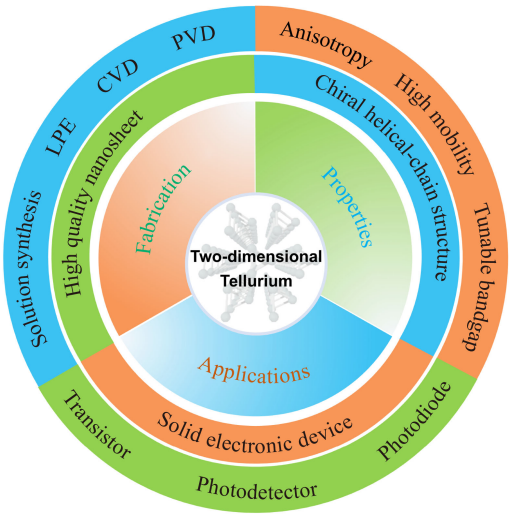

Keywords two-dimensional materials, tellurium, van der Waals heterostructure, electronic, optoelectronic

Contents

*Special Topic: Two-dimensional Materials for Optoelectronics (Eds.: Tianyou Zhai & Xing Zhou).

Higher Education Press

https://doi.org/10.1007/s11467-022-1231-9

1 Introduction

Over the past decade, two-dimensional (2D) materials, such as graphene, transition metal dichalcogenides (TMDs), black phosphorus (BP) and hexagonal boron nitride (h-BN), have inspired explosive research interests in academic and industrial world [1–13]. Compared with conventional 3D materials, 2D materials are only a few atomic layers thick, which endow them various unusual optical, electronic, magnetic, thermal and mechanical properties [14–17]. As results, 2D materials have displayed significant potential for numerous applications like electronics, optoelectronics, spin-electronics, energy conversation and storage, biomedicine, sensors, environments, etc. [18–29]. Especially, the rich structures, high carrier mobility, tunable bandgap and strong light-matter interactions of 2D materials enable them one of the most promising candidates for building high-performance electronic and optoelectronic devices [30–35]. To date, 2D material-based field effect transistors (FETs) have achieved a leap forward in small size and low power consumption, which are expected to further extending the Moore's law [36]. Moreover, the 2D photodetectors with high sensitivity, fast response speed, low noise, and wide response range have been widely explored [37–47]. To further expand the research in these fields, exploring new 2D materials with superior properties and building their novel multifunctional devices are the key projects in the 2D field.

Tellurium (Te), a novel single-element 2D material, has attracted great research interest owing to its unusual chiral helical-chain structure and accompanying novel optical and electrical properties [48, 49]. The scarce p-type conduction feature together with the ultra-high carrier mobility (up to 1000 $cm^2 \cdot V^{-1} \cdot s^{-1}$ at room temperature) of 2D Te make it an ideal candidate for building high-performance electronic devices [50]. The bandgap of 2D Te can be continuously modulated from 0.31 to 1.26 eV with the thickness down from bulk to single layer, this wide-tunable bandgap enables 2D Te applicable to construct the broadband photodetectors [51]. The dangling-bond-free surface of 2D Te also allows the design of heterostructures with atomic-level resolved interfaces with diverse energy band alignments between different 2D materials, which would bring many novel properties and applications [52–55]. Moreover, the significant linear dichroism, photoconductivity, thermoelectricity, nonlinear optical response, piezoelectricity, and topology properties of 2D Te provide it considerable opportunities to fabricate novel multifunctional electronic and optoelectronic devices such as modulators, logic devices and polarization-sensitive photodetectors [56–64]. Importantly, the capable of large-scale synthesis and the better stability of 2D Te endow it great possibility to realize the above device applications.

Although there are some early reviews have described the research progress of 2D Te [65–68], the demand for different functions of Te stimulate the booming development of various synthesis techniques. In addition, new type of Te-based electronic and optoelectronic devices have been further researched and developed during these two years. Especially, in the wake of the deepening of Te research, many new challenges and opportunites ahead for researchers, which will further motivate us to devote persistent efforts. Hence, a timely comprehensive review is of special significance to afford the latest advances and perspectives about this attractive material.

In this review, we give a systematical summary to the research progress of 2D Te in recent years as schematically shown in Fig. 1. Initially, we briefly introduce the structure features, basic physical properties, and various preparation methods of 2D Te. Additionally, we emphatically introduce the booming electronic and optoelectronic applications of 2D Te including FETs, photodetectors and van der Waals heterojunction (vdWH) photodiodes. Finally, current challenges and future perspectives regarding the property exploration, controlled preparation and device application of 2D Te are discussed.

2 Structure and properties of tellurium

2.1 Atomic structure

Combining first-principles calculation and experiment, researchers found that Te should has three phase structures, including the hexagonal α-Te, the tetragonal β-Te and the γ-Te, as shown in Figs. 2(a)–(c) [69]. Due to the differences in cohesion energy (2.62 eV/atom for α-Te, 2.56 eV/atom for β-Te and 2.46 eV/atom for γ-Te) and phonon spectra, α-Te is the most stable phase structure of few-layer Te at equilibrium state, and it can transform into β phase when thickness reduces to the monolayer limit [70]. The crystal structure of Te is composed of Te atomic chains in a triangular helix that stacked together

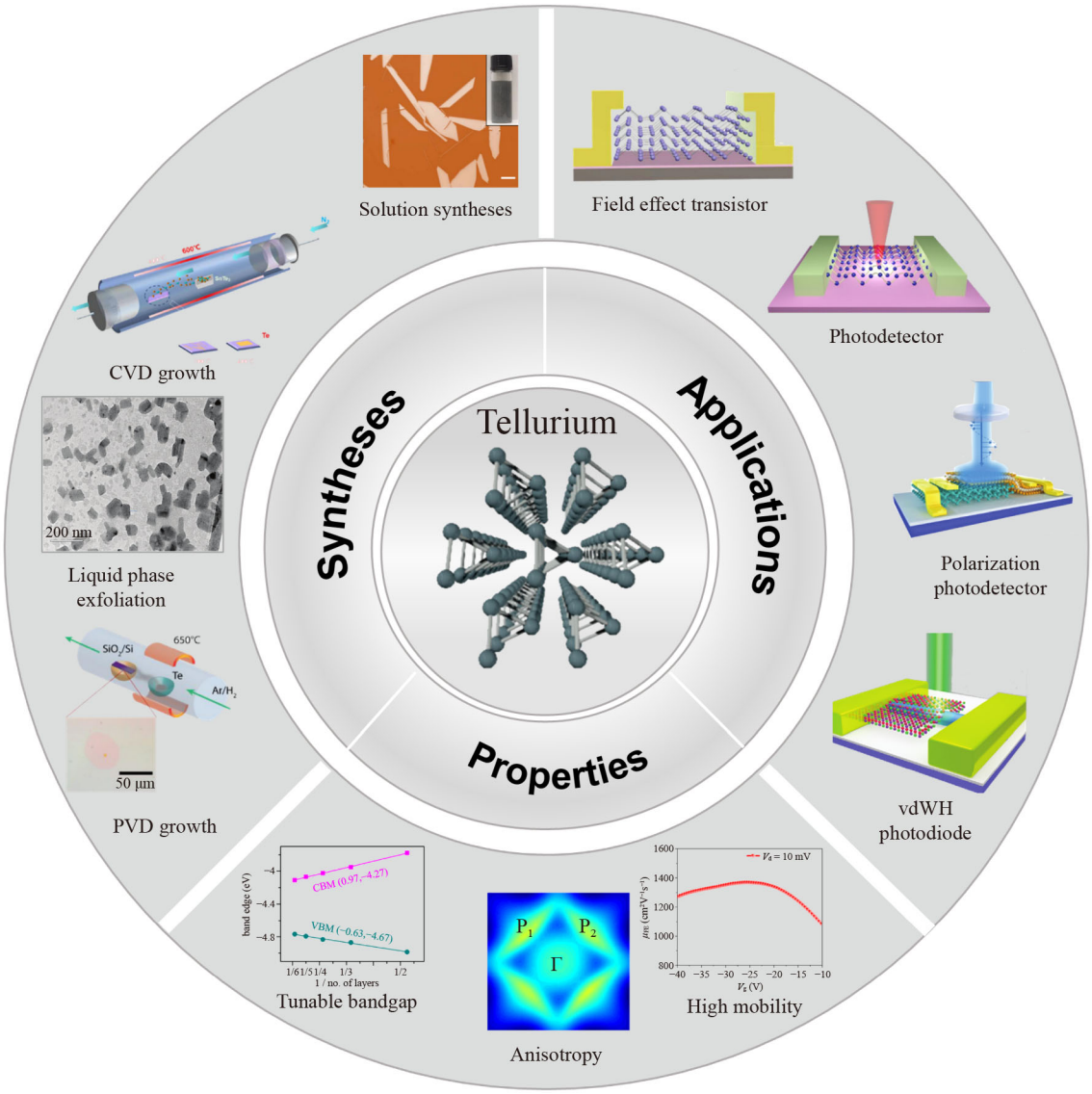

Fig. 1 Overview of low-dimensional tellurium showing the fabrications, properties, and relevant device applications.

via vdW forces in a hexagonal array, and Te atoms form covalent bonds with only the two nearest neighbor Te atoms in the helical chain [Figs. 2(d)–(f)] [71]. The unique in-plane asymmetric chiral chain structure of Te crystal endows it strong anisotropic properties and many novel physical properties that are different from those of conventional 2D materials. Moreover, the quasi-1D structure feature of Te make it can not only form into the 2D vdW crystal, but also form into the 1D vdW crystal, as discussed in the preparation section [72].

2.2 Physical properties of tellurium

As an emerging member of 2D materials family, 2D Te has received considerable theoretical and experimental studies for exploring its physical properties. It was found that Te possesses excellent physical properties including tunable bandgap, high carrier mobility, strong anisotropy, and better stability.

2.2.1 Bandgap and carrier mobility

Density functional theory (DFT) has been used to explore the electronic band structure of monolayer and few-layer Te crystal. It was found that the bandgap of 2D Te crystal can be significantly modulated via tuning its thickness [73]. Figure 3(a) presents the irreducible Brillouin zone (BZ) of Te crystal, where the bandgap is located at the H point. Theory calculations show that bulk Te is a nearly direct bandgap semiconductor with a bandgap of 0.31 eV [Fig. 3(b)], while bilayer Te is an indirect bandgap semiconductor with bandgap of 1.17 eV [Fig. 3(c)]. As shown in Fig. 3(d), the band-edge energy (conduction-band minimum (CBM) and valence-band maximum (VBM)) of Te crystal shows linear evolution as a function of thickness variation [74].

Owing to the thickness-tunable bandgap, 2D Te holds great promise for wide-band optical detection. Using

DFT calculations, Wu *et al.* and Qiao *et al.* [70, 73] studied the light absorption of different layers β-Te and α-Te, respectively. As shown in Fig. 3(e), the light absorption coefficient of β-Te shows obvious decrease with the thickness increase, and its absorption range covers from 100 to 2000 nm. For α-Te, the absorbances are roughly 2%–3% per layer at 1.6 eV and 6%–9% at 3.2 eV, which are nearly twice to three-times those of

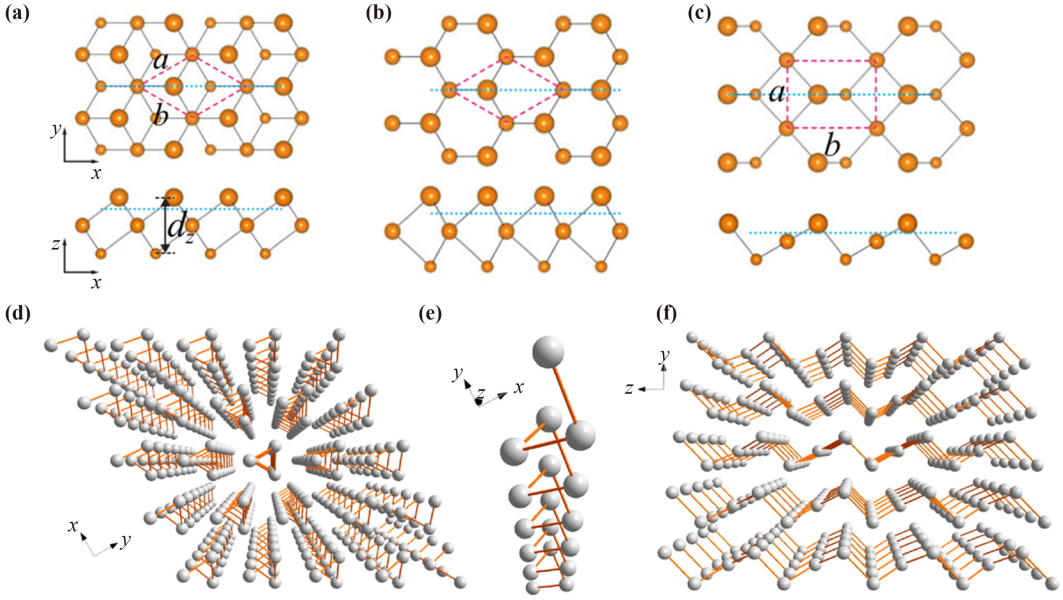

Fig. 2 Schematic diagram of the structure of Te crystal. **(a–c)** Top and side views of Te in different phase structures: (a) α-Te, (b) γ-Te and (c) β-Te [69]. **(d–f)** Atomic structures of Te (d) viewed from the x-axis, (e) single molecular chain, and (f) viewed from the z-axis [71].

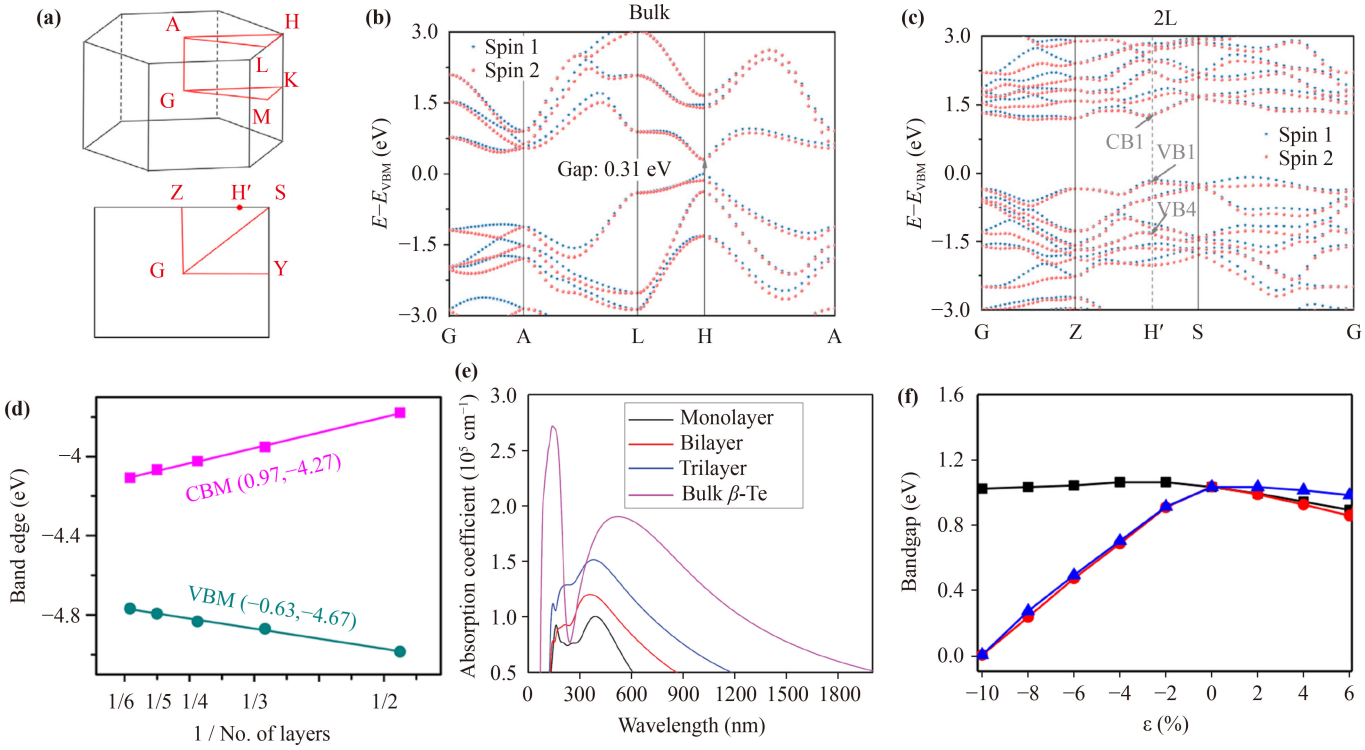

Fig. 3 Tunable bandgap. **(a)** Brillouin zone of bulk and few-layer α-Te. Energy band structure of **(b)** bulk and **(c)** bilayer α-Te [73]. **(d)** Band-edge energy of CBM and VBM as function of layer numbers [74]. **(e)** Calculated light absorption coefficient of bulk, few-layer and monolayer β-Te [70]. **(f)** Bandgap as a function of the biaxial strain (red line with circles), uniaxial strains along armchair (black line with squares) and zigzag (blue line with triangles) directions, respectively [79].

BP. In experiments, Peng *et al.* [75] measured the absorption spectrum of 2D Te, where the absorption cutoff wavelength is about 0.35 eV, consistent well with the theory results. Note that the narrow optical bandgap of 2D Te allows it to be utilized for broadband photodetection. In addition, researchers have also simulated the absorption spectra of Te nanosheet and nanowire by using the time-domain finite difference method, and found that the morphology of Te crystal has a slight affect to its light absorption.

As well known that applying strain to semiconductors is an easy-to-implement routine method for tuning their energy band structure [76–78]. In this regard, it would be possible to further modulate the bandgap of 2D Te via applying strain. Zhu *et al.* [79] calculated the band structure of 2D Te under the biaxial strains as shown in Fig. 3(f). It is found that CBM shifts down gradually towards the Fermi Level as the tensile strain increases from 0% to 6%, whereas VBM almost does not change, resulting in the bandgap reduction. Moreover, applying a compress strain on 2D Te can also modulate its energy band structure. Notably, the manner of strain applied on 2D Te has significant effect on its bandgap modulation. For example, the tensile strain applied along the armchair direction of Te crystal shows more significant modulation to the bandgap of Te than that along the zigzag direction [Fig. 3(f)]. On the other hand, monolayer Te undergoes a direct-to-indirect bandgap transition under the compressed strain, which could greatly improve its light absorption and thus expanding the scope of optoelectronic applications.

Carrier mobility, which reflects the rate of electrons and holes movement in a solid material, is another key intrinsic property of 2D semiconductors that determines whether they are promising for application in electronic devices. Zhu *et al.* [80] estimated the carrier mobility of Te using the phonon finite method. The calculated effective mass of electron and hole are $m_{\mathrm{e}}^{*} = 0.47\ m_{\mathrm{e}}$ and $m_{\mathrm{h}}^{*} = 0.58\ m_{\mathrm{e}}$, respectively, indicating that Te may possess high electron and hole mobilities. In experiment, researchers do achieve the high carrier mobility of 2D Te, the room temperature carrier mobilities can up to hundreds to thousands of $\mathrm{cm^2 \cdot V^{-1} \cdot s^{-1}}$ [50]. Qiao *et al.* [73] found that the carrier mobility will increase with increasing layer thickness, the hole mobility along the *y*-direction in 5 and 6 layers is very large, while the electron mobilities are generally 1–2 orders of magnitude smaller than the hole mobilities, and the mobilities along the *z*-direction are generally smaller than that along the *y*-direction.

2.2.2 Anisotropy property

The properties of 2D materials are closely related to their lattice symmetry. Compared to the high isotropy of high-symmetry 2D materials, low-symmetry 2D materials usually exhibit strong in-plane anisotropic properties, which provide more degree of freedom for building novel multifunctional devices [81–83]. As demonstrated above, Te crystal possesses a quasi-1D chiral helical-chain structure with strong covalent bonds in *z*-axis and vdW interaction in *x* and *y*-axis, which introduces it an intrinsic geometric anisotropy. Xian *et al.* [84] calculated the energy band structure of Te crystal by considering spin-orbit coupling (SOC). The results show a Dirac-cone-like dispersions exist at P1 (along the ΓM1 direction) in the BZ as indicated by the blue boxes in Fig. 4(a). Clearly, the energy band profile around P1 show that the band dispersions are highly anisotropic [Fig. 4(b)]. Qiao *et al.* [73] calculated the absorption spectra of Te crystal with different layers along the *x*, *y* and *z* directions. Taking the bilayer Te as an example, the absorbance measured under incident light linearly polarize along *y* and *z* directions is larger than that along *x* direction. In addition, Wang *et al.* [56] studied the anisotropic optical properties of 2D Te by measuring the differential reflection (ΔR) at different sample direction θ, as shown in Fig. 4(d). Clearly, the ΔR show a pronounced angle dependence, the maximum and minimum values are obtained when θ equals 90 and 0°, respectively. Angle-resolved polarization Raman spectroscopy was also utilized to reveal the anisotropy of 2D Te as shown in Fig. 4(e) [50]. Clearly, the four primary Raman peaks located at 94, 105, 125 and 143 $\mathrm{cm^{-1}}$ show periodic variation with polarization angle modulate from 0 to 180°, suggesting strong in-plane anisotropy of Te. Furthermore, DFT calculation has confirmed that the effective carrier mass of both electron and hole in different lattice directions of Te crystal show obvious difference [79], suggesting the strong anisotropic electrical transport properties. The above results demonstrate that 2D Te with strong optical and electrical anisotropy is beneficial to develop novel optoelectronic devices.

2.2.3 Stability

As a new 2D material, the structure and environmental stability of Te is a key issue for its applications. Zhu *et al.* [79] studied the kinetically thermodynamic stability of Te via theory calculation. Figure 5(a) shows the phonon band dispersions of Te and the displacement patterns corresponding to the six optical modes of the Γ point, which illustrate the different characteristics of bond stretching and bending. Clearly, there is no soft phonon modes in the computed phonon dispersion spectrum of Te, suggesting that the Te is kinetically stable. Moreover, they also investigated the thermodynamic stability of Te using the ab initio molecular dynamics (MD) calculations at finite temperature, and found that the equilibrium structures of *α*-Te and *β*-Te are very stable up to room temperature, while *γ*-Te became unstable at about 200 K. Take *β*-Te as an example, its

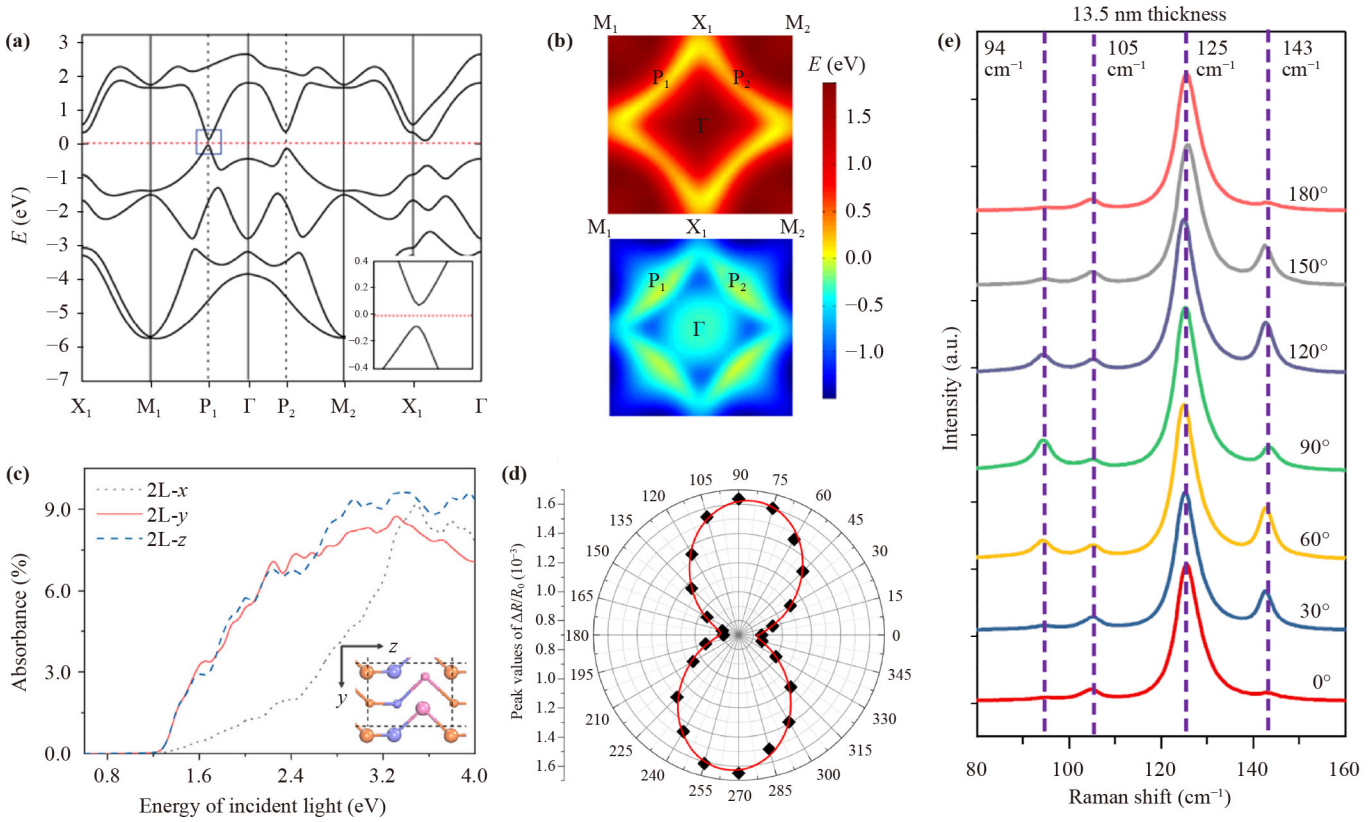

Fig. 4 **(a)** Band structure of square Te. Inset: Zoom-in of the band structure in a small region around the semi-Dirac cone at P_1 as indicated by a blue box. **(b)** Band contour for the bottom conduction band (upper panel) and the top valence band (lower panel) in the first BZ. Bottom. SOC is included for all results [84]. **(c)** Optical absorption spectra of 2L-α-Te as a function of the polarization direction of the incident light along x, y and z [73]. **(d)** Peak differential reflection signal as a function of θ which is the angle between the long side of the sheet and the horizontal direction in the laboratory configuration [56]. **(e)** Angle-resolved polarization Raman spectra of 2D Te (thickness: 13.5 nm) [50].

atomic structure shows a tiny change at room temperature, revealing the high structural rigidity [Fig. 5(b)]. To access the air-stability of Te, Qiao *et al.* [73] studied the interaction between α-Te and O_2 or H_2O molecule. Fig. 5(c) shows the schematic atomic structure of physisorbed O_2 [Fig. 5(c) left] and H_2O [Fig. 5(c) middle] on bilayer α-Te as well as the energy potential of physisorbed O_2 on bilayer α-Te in the most stable configuration [Fig. 5(c) right]. It can be found that the energy barrier of O_2 adsorbed on bilayer α-Te can up to 0.85 eV and even to 0.94 eV, which is sufficient to prevent α-Te being oxidized at ambient conditions. For H_2O, its adsorption energy on bilayer α-Te is –0.29 eV, several tens of meV stronger than that on BP and the intermolecular interaction energy of H_2O, which results in α-Te slightly hydrophilic (contact angle of 76°).

2.2.4 Chiral property

2D Te crystal possesses an unusual chiral helix-chain structure, which result in complex band structures with Weyl crossings and unique spin textures that bring novel gyrotropic properties. As early as 1960, Nomura discovered the strong optical rotatory power of Te via measuring levo- and dextrorotatory Te crystal by single-beam double-pass infrared spectrometer [85]. Asnin *et al.* [86] forecasted a novel circular photogalvanic effect in Te via theory calculations, which deserve further exploration in experiment. Moreover, the current-induced electronic magnetization effect was observed in bulk Te by using nuclear magnetic resonance measurements [87]. This effect is attributed to spin splitting of the bulk band owing to the lack of inversion symmetry in trigonal Te. In addition, the lack of mirror and inversion symmetries also result in a unique radial spin texture in the Te band structure. Recently, the all-electrical generation, manipulation, and detection of chirality-dependent spin polarization were achieved in single-crystalline Te nanowires by recording a large and chirality-dependent unidirectional magnetoresistance [88]. The orientation of the electrically generated spin polarization is determined by the nanowire handedness and uniquely follows the current direction, while its magnitude can be manipulated by an electrostatic gate. What's more, the topological phase transition from a trivial semiconductor to a Weyl semimetal is under applied external pressure when the

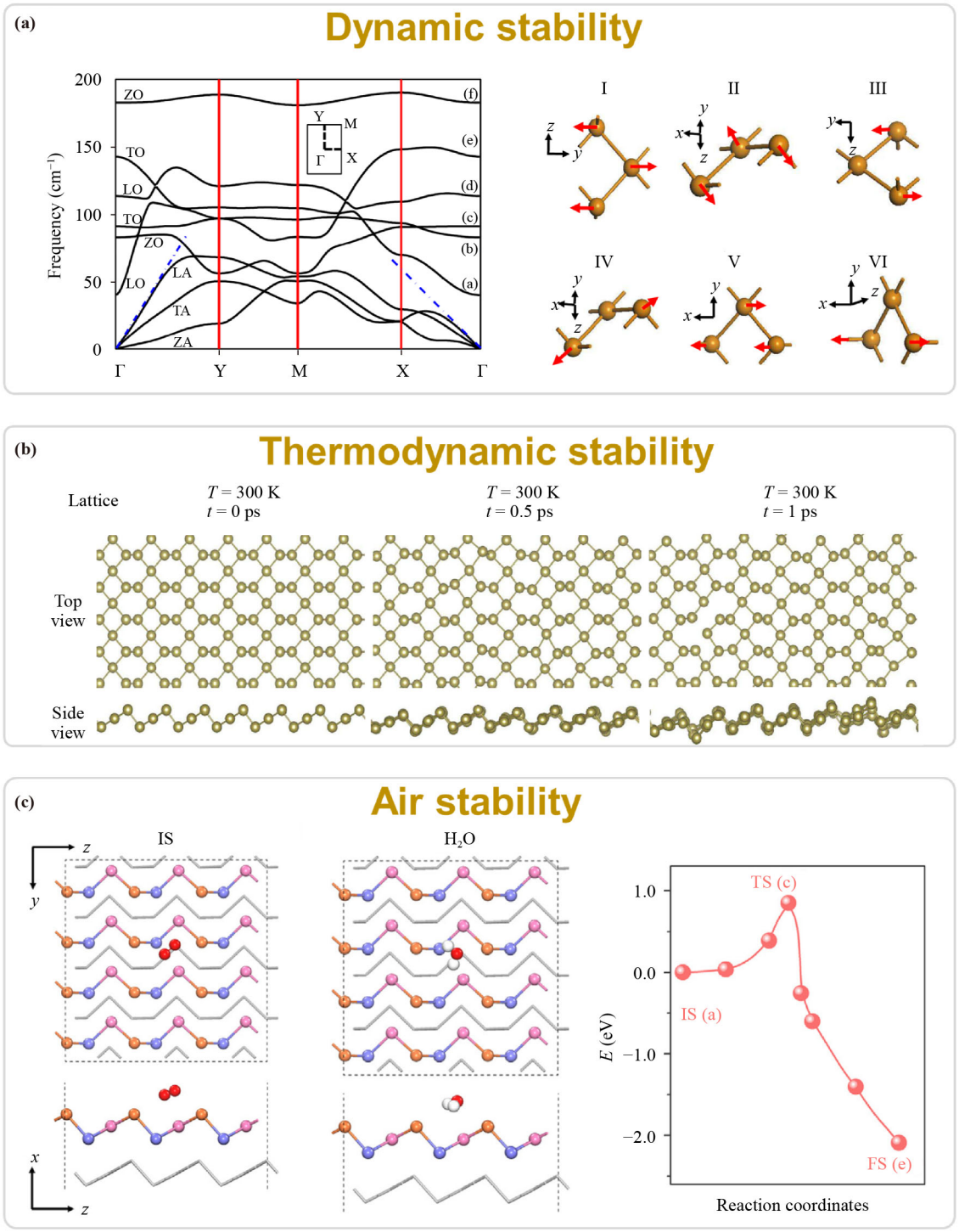

Fig. 5 **(a)** Phonon band dispersions of Te crystal (left panel) and the corresponding displacement patterns of the six optical modes at Γ point: ZA, TA, LA, TO, LO and ZO (right) [79]. **(b)** Snapshots of ab initio MD simulations of monolayer Te annealing at temperature of 300 K for 0, 0.5 and 1 ps [79]. **(c)** Atomic structures of physisorbed O_2 and H_2O on bilayer α-Te (left) and energy profile of the reaction pathway for O_2 on α-Te (right) [73].

spin-polarized uppermost valence bands and conduction band are inverted across the bandgap [89, 90]. As demonstrated above, 2D Te provides an ideal platform for exploring novel chiral-related polarization optics, multiferroics, and spintronics.

3 Preparation approach of tellurium

The controlled preparation of 2D Te with desirable size, morphology, thickness, and crystal quality is significant for the investigation of their properties and potential

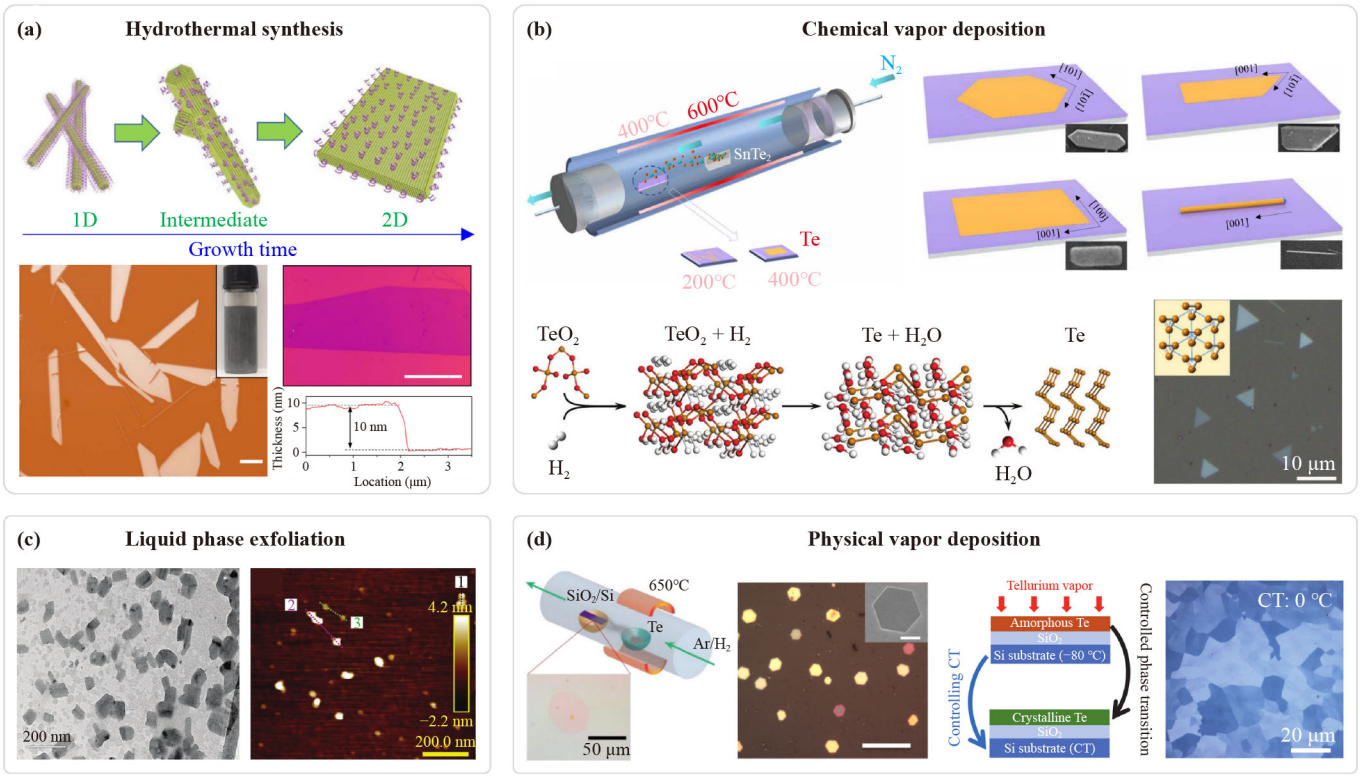

Fig. 6 **(a)** Schematic diagram of hydrothermal synthesis of Te nanosheets and the morphological evolution from 1D Te structures to 2D Te structures (top); optical images of solution-grown Te nanosheets (bottom left), scale bar is 20 μm. Inset is the digital photograph of Te solution dispersion; AFM image of a typical 2D Te nanosheet and the corresponding height profile, scale bar is 1 μm (bottom right) [50]. **(b)** Schematic diagram of the CVD growth of low-dimensional Te crystal with $SnTe_2$ as Te precursor and the corresponding morphology of Te grown at different temperatures (top); schematic diagram of the CVD growth process with TeO_2 as Te precursor (bottom), and the OM image of obtained 2D Te nanosheets [75, 107]. **(c)** TEM and AFM image of liquid phase exfoliated Te nanosheets [102]. **(d)** Schematic diagram of PVD growth of 2D Te nanosheets (first from left); OM image of 2D Te hexagonal nanoplates, scale bar is 30 μm (second from left); schematic of the controlled phase transition process (second from right); polarized light microscopy image of the Te films (10 nm) crystallized at 0 °C (first from right) [111, 112].

applications. Many synthesis methods have been developed to obtain high-quality Te nanostructures with different morphologies, including solution synthesis, liquid phase exfoliation, chemical vapor deposition and physical vapor deposition.

3.1 Solution synthesis

The low-dimensional Te reported in most of works are prepared by the solution synthesis method which is a relatively simple method that have been used to synthesize various 2D TMDs in large-scale [91–93]. The solution synthesis of low-dimensional Te crystal was achieved via a reduction reaction between Na_2TeO_3 and hydrazine hydrate, and the polyvinylpyrrolidone was used to turn the morphology of Te. During the synthesis process, Te goes through a gradual transition from 1D nanowire to 2D nanosheet with increasing time, as schematically shown in Fig. 6(a) [50]. This morphology evolution process is mainly due to the balance between kinetic and thermodynamic growth that determines the structural transition. So, we can selectively prepare the 2D Te nanosheets via prolong the synthesis time. At the initial growth stage, the products are primary 1D nanostructures, then the 1D Te nanostructure gradually transform into 2D Te nanostructure. Finally, 2D Te flakes were obtained with the reaction time extending. The obtained 2D Te nanosheets have better dispersibility in deionized water, which is beneficial to fabricate the flexible electronic devices via ink-jet printing [94–96]. The domain size of obtained Te nanosheets, with average thickness about 10 nm, is in the range of 10–50 μm. Moreover, the Te nanosheets have relative high crystal quality and better air stability. Thus, Te nanosheets synthesized by solution method have been widely utilized to fabricating electronic and optoelectronic devices reported recently [71, 97, 98]. Usually, few Te nanowires are mixed with the 2D Te nanosheets, but they can be removed by centrifugation.

3.2 Liquid-phase exfoliation

Liquid-phase exfoliation (LPE) is a powerful method for

the scaled-up fabrication of ultrathin nanosheets form bulk layered materials. Dispersing them in solvent is a direct and effective way to reduce the interlayer vdW force, which allows the LPE method possible to achieve industrialization and commercialization due to its high-yield mass production [99–101]. Xie *et al.* [102] for the first time, obtained ultrathin 2D Te nanosheets using LPE. Firstly, Te powder was dissolved in isopropyl alcohol solvent, and then the mixture was transferred to a plastic tube followed by probe sonication at 200 W ultrasonic power. Finally, the mixture was further subjected to water-bath sonication at 400 W power to obtain 2D Te nanosheet solutions. Transmission electron microscopy (TEM) and atomic force microscope (AFM) images [Fig. 6(c)] of 2D Te nanosheets obtained by LPE show the lateral dimension in a broad range from 41.5 to 177.5 nm with thicknesses ranging from 3.4 ± 0.3 to 6.4 ± 0.2 nm. Obviously, the preparation of Te nanosheets via LPE has a relatively poor controllability including the size and thickness, especially, the grain size is much small, which are unfavorable to its device applications. We suggest that several factors including ultrasonic energy, favorable anisotropic characteristics and solvent-nanosheet interactions of bulk materials should be considered in future LPE preparation for improving the stripping efficiency and controllability.

3.3 Chemical vapor deposition

Chemical vapor deposition (CVD) is one of the representative bottom-up approaches for fabricating traditional semiconductor films and various 2D layered and nonlayered materials [103–105]. Recent years, CVD growth has also been utilized to prepare high-quality 2D Te in large-scale. Figure 6(b) (top left) shows the schematic diagram of CVD preparation of Te where $SnTe_2$ powder was used as the Te source and Si was used as growth substrate [75]. It was found that the Te crystals grown at different temperatures show different morphologies. As shown in Fig. 6(b) (top right), 2D Te nanosheets with the length and thickness ranging from 20 to 80 μm and 20 to 200 nm, respectively, were grown at 400 °C. In contrast, 1D Te nanowires with length ranging from 10 to 50 μm and diameter around 200 nm are obtained at 200 °C. This is reasonable as the Te crystal itself possesses the intrinsic quasi-1D structure. At the low-temperature region, the Te crystal preferentially grow into 1D nanowire due to the low surface energy of Te in [001] direction. At the middle- and high-temperature regions, 2D Te nanosheets are primarily obtained. Notably, the Te nanosheets grown at the middle-temperature region are mostly rectangular morphology, while that grown at the high-temperature region are primarily pentagonal or hexagonal morphology. Clearly, tuning the growth temperature should be an effective way to controllably synthesize 1D and 2D Te. Beside $SnTe_2$, In_2Te_3 was also utilized as Te precursor for CVD growth of Te crystals [106]. Notably, such metal Te precursors would introduce extra elements into the growth system, which is unfavorable to the growth of high-quality 2D Te. Zhai *et al.* [107] reported synthesis of 2D Te flakes on mica substrate using CVD growth with TeO_2 as Te precursor and H_2 as the reducing atmosphere. The as-grown 2D Te flakes have regular triangle morphology with a uniform thickness of only 5 nm as shown in Fig. 6(b) (bottom right). It needs to be note that the H_2 plays a key role in the growth process of 2D Te as schematically shown in the bottom left of Fig. 6(b). The presence of H_2 promotes the formation of an intermediate transition state (denoted as $TeO_2 + H_2$) that induced by a hybrid action of O 2p of TeO_2 and H 1s of H_2. In addition, the formation of H_2O as an intermediate product at the stage of another intermediate transition state ($Te + H_2O$) is conducive to the frame composed of Te atoms and ultimately 2D layered Te flakes formation. All in all, CVD growth is a convenient and effective method for the large-scale preparation of high-crystal 2D Te. Of course, it is still challenging to precisely control over the thickness and morphology of the 2D Te film.

3.4 Physical vapor deposition

Physical vapor deposition (PVD) is another typical bottom-up method for the preparation of 2D materials. PVD growth usually requires high purity source as well as high vacuum environment, the solid or liquid precursors evaporate in the form of atoms or molecules, and then transports to the target substrate where it condenses or deposits [108–110]. As Te is a single-element 2D materials, PVD growth was recently widely used to synthesize 2D Te nanosheets. Apte *et al.* [111] reported the synthesis of 2D Te nanosheets via PVD growth as shown in Fig. 6(d) (first from left). Pure Te bulk as precursor is placed in a quartz boat at the high temperature zone, and SiO_2/Si substrate is located at the low temperature growth zone. The growth of 2D Te flakes were achieved at 450 °C for 30 min with Ar as carrier gas. The obtained Te flakes have a thickness of 0.85 nm, corresponding to three atomic layers [Fig. 6(d) second from left]. Moreover, Zhao *et al.* [112] explored the kinetics and dynamics of the crystallization of thermally evaporated Te films for its large-area single-crystal preparation. They found that thermally evaporated Te possesses an intriguing crystallization behavior, where an amorphous to crystalline phase transition happens at near-ambient temperature. By controlling the crystallization process, the authors demonstrated the low-temperature processing of highly crystalline Te films with large grain size and preferred out-of-plane orientation ((100) plane parallel to the surface). As results, large-area 2D Te film with crystalline grain size up to 6 μm are prepared on various substrates including glass and plastic. Lu *et al.* [113] reported the synthesis of 2D Te films on pre-patterned SiO_2/Si substrate by using pulse-laser-assisted PVD.

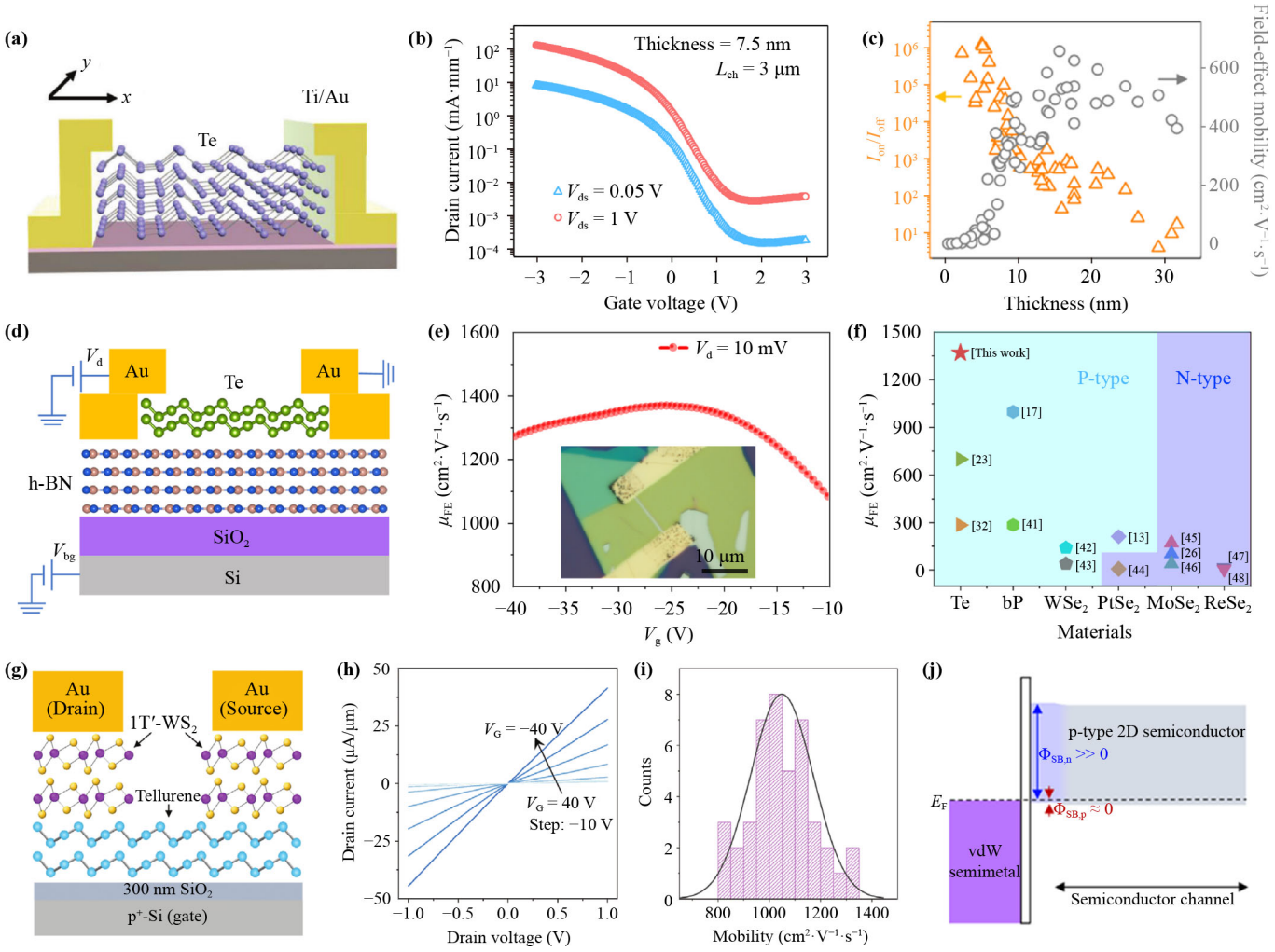

Fig. 7 **(a)** Schematic diagram of structure 2D Te-based FET [130]. **(b)** Transfer curve of a typical long-channel 2D Te-based FET with a thickness of 7.5 nm. **(c)** Statistic on/off ratio (orange triangles) and carrier mobility (gray circles) of 2D Te-based FET as a function of thickness [50]. **(d)** Schematic illustration of Te-based FET with global bottom-gate structure on h-BN/SiO_2/Si substrate. **(e)** Carrier mobility of 2D Te-based FET extracted from the transfer curves under the bias voltage of 10 mV. Inset: Optical image of a typical Te-based FET on h-BN/SiO_2/Si. **(f)** Summary of carrier mobility of the Te crystal and other 2D materials reported in literature [117]. **(g)** Device structural diagram of 2D Te-based FET with the semimetal 1T′-WS_2 as contacts. **(h)** Output curves of the 2D Te-based FET under different gate voltage. **(i)** Statistical carrier mobility distribution of the 2D Te-based FETs. **(j)** Band structures of all-vdW semimetal-semiconductor contacts, where $\Phi_{SB,n}$ and $\Phi_{SB,p}$ refer to Schottky electron barrier and Schottky hole barrier, respectively [127].

They obtained centimeter-scale 2D Te films with uniform thickness and high crystal quality. Moreover, molecular beam epitaxy, a PVD approach with more precise control, was used to synthesize 2D Te film on various substrates such as mica, graphene and germanium [114]. Hence, PVD growth offers a large freedom for modulate the crystal quality, thickness, and size of 2D Te nanosheets, which is beneficial to promote the Te-based optoelectronic device applications.

4 Tellurium-based electronic and optoelectronic devices

Owing to the high carrier mobility, p-type conductor feature and wide-tunable bandgap, 2D Te is considered as one of the most promising candidates for building high-performance electronic and optoelectronic devices. In this section, we primarily discuss the recent research progresses of Te-based electronic devices and photodetectors.

4.1 Tellurium-based electronic devices

FET is an important electronic component in integrated circuits. In order to further extend the Moore's law, 2D materials (such as graphene, BP, and TMDs) which can effectively avoid the short-channel effect, have been widely used as semiconductor channel to replace the traditional Si channel [115, 116]. As discussed above, the

excellent physical properties of 2D Te together with the capable of large-scale preparation enables it an ideal candidate for building high-performance FETs. Figure 7(a) presents the schematic structure of Te-based FETs. In 2018, Wang *et al.* [50] for the first time explored the electrical transport properties of solution-synthesized 2D Te FET. The device exhibits a p-type conductor feature with slight bipolar due to the narrow bandgap of Te [Fig. 7(b)]. Moreover, the on-off ratio of the device is about 10^6 and the carrier mobility up to 700 $cm^2 \cdot V^{-1} \cdot s^{-1}$ at Te thickness of 16 nm [Fig. 7(c)], which is better than most of conventional 2D materials. However, the mobility greatly reduces with the thickness decreasing due to the susceptibility of thinner Te nanosheet to the interfacial charge impurities and surface scattering.

In view of this, Yang *et al.* [117] reported the direct growth of high-quality Te nanoribbons on atomically flat h-BN substrate and the fabrication of high-performance Te-based FET, as shown in Fig. 7(d). The h-BN dielectric substrate not only provides a dangling bond-free ultra-flat surface for the growth of high-quality Te nanoribbons, but also reduces scattering centers at the interface between the channel material and the dielectric layer. As results, the FET device achieved an ultra-high hole mobility up to 1370 $cm^2 \cdot V^{-1} \cdot s^{-1}$ at room temperature [Fig. 7(e)], this value is higher than that of the well-known 2D TMDs [Fig. 7(f)]. In addition, Qin *et al.* [118] prepared BN-encapsulated Te nanowires via physical vapor transport method, the diameter of Te nanowires can be modulated by controlling the inner diameter of BN nanotubes. Compared with bare Te nanowires on SiO_2, BN-encapsulated Te nanowires exhibit a dramatically enhanced current-carrying capacity with a current density of 1.5×10^8 $A \cdot cm^{-2}$ which exceeds that of most semiconducting nanowires. Moreover, to further improve the performance of Te-based FETs, alumina-encapsulated 2D Te film was prepared via magnetron sputtering at low temperature of 150 °C [119]. The aluminum oxide (Al_2O_3) encapsulation layer assists the growth of hexagonal Te crystals by stabilizing the interface and enlarge the crystal size of Te film, resulting in greatly improved FET performance. Compared to the unpackaged device, the off-current is reduced by a factor of more than 70, enabling an on-off ratio of 5.8×10^5 and a subthreshold swing of 6.5 $V \cdot dec^{-1}$.

Improving the contact between semiconductor and metal electrode is also an effective means to enhance the FET performance. Due to the Fermi level pinning effect and the metal induced gap of metal electrodes, semiconductor devices are easily plagued by high Schottky barriers of metal-semiconductor contacts, especially for p-type semiconductors [120]. 2D materials with atomic-scale thickness are more susceptible to contact interface traps, lattice defects and chemical interactions [121–125]. Therefore, in order to construct high-performance Te-based FETs, it is necessary to design suitable electrode contacts to lower the Schottky barrier. Recently, Wang *et al.* [126] calculated the interfacial properties between Te and a series of 2D metals by first-principles calculations. They found that the metallic 2D NbS_2 and TaS_2 can form p-type ohmic contacts with monolayer α-Te, suggesting that 2D metal as contact electrode may be beneficial to building high-performance Te-based FETs. In experiment, Zhang *et al.* [127] designed a Te-based FET with full vdW contacts by using the 2D semimetal 1T'-WS_2 as contact electrodes, as schematically shown in Fig. 7(g). The output characteristic curve of the device shows good linearity, indicating that an ohmic contact is formed between electrode and Te [Fig. 7(h)]. Moreover, the Te-based FET exhibit a much high hole mobility up to 1304 $cm^2 \cdot V^{-1} \cdot s^{-1}$ [Fig. 7(i)], indicating the great improvement of the device performance via the contact optimization. The device performance enhancement is attributed to the high work function (4.95 eV) of the semimetal 1T′-WS_2, which matches well with the VBM of Te [Fig. 7(j)], forming a near-zero Schottky potential base. Moreover, similar performance improvements were achieved by choosing semimetal $PdTe_2$ and $PtTe_2$ as contact electrodes of the Te-based FET [128, 129]. From the above research works, we can see that the Te-based FET exhibit excellent performance including ultrahigh mobility and large on-off ratio, and that can be further improved by improving the material quality as well as optimizing the electrode contact.

4.2 Tellurium-based photodetectors

Owing to the strong light-matter interaction, wide-tunable bandgap, and air stability of 2D Te, it has been widely utilized to building broadband photodetectors. In general, the photocurrent generation mechanisms of 2D Te-based photodetectors are photoconductive, photogating or photo-thermoelectric effects. The metrics to evaluate the performance of photodetectors including responsivity (R), specific detectivity (D^*), response spectrum range, response time, external quantum efficiency (EQE), photoconductive gain (G) and noise equivalent power (NEP). In the following subsections, we systematically introduce the booming development of 2D Te-based photodetectors.

Since Te is a heavily doped narrow bandgap semiconductor with superior conductivity and heavy atomic mass, Te has excellent thermoelectric properties and thus can be developed as a thermoelectric device [58, 131]. Recently, Qiu *et al.* [132] reported a Te-based photodetector working by the photo-thermoelectric effect. Figure 8(a) shows the schematic diagram of the device structure, where the thermoelectric current generates between the two metal contacts via locally heating the Te channel with a 633 nm laser to create temperature gradient. When the laser illuminates the left side of the channel, the local temperature of this side will be higher

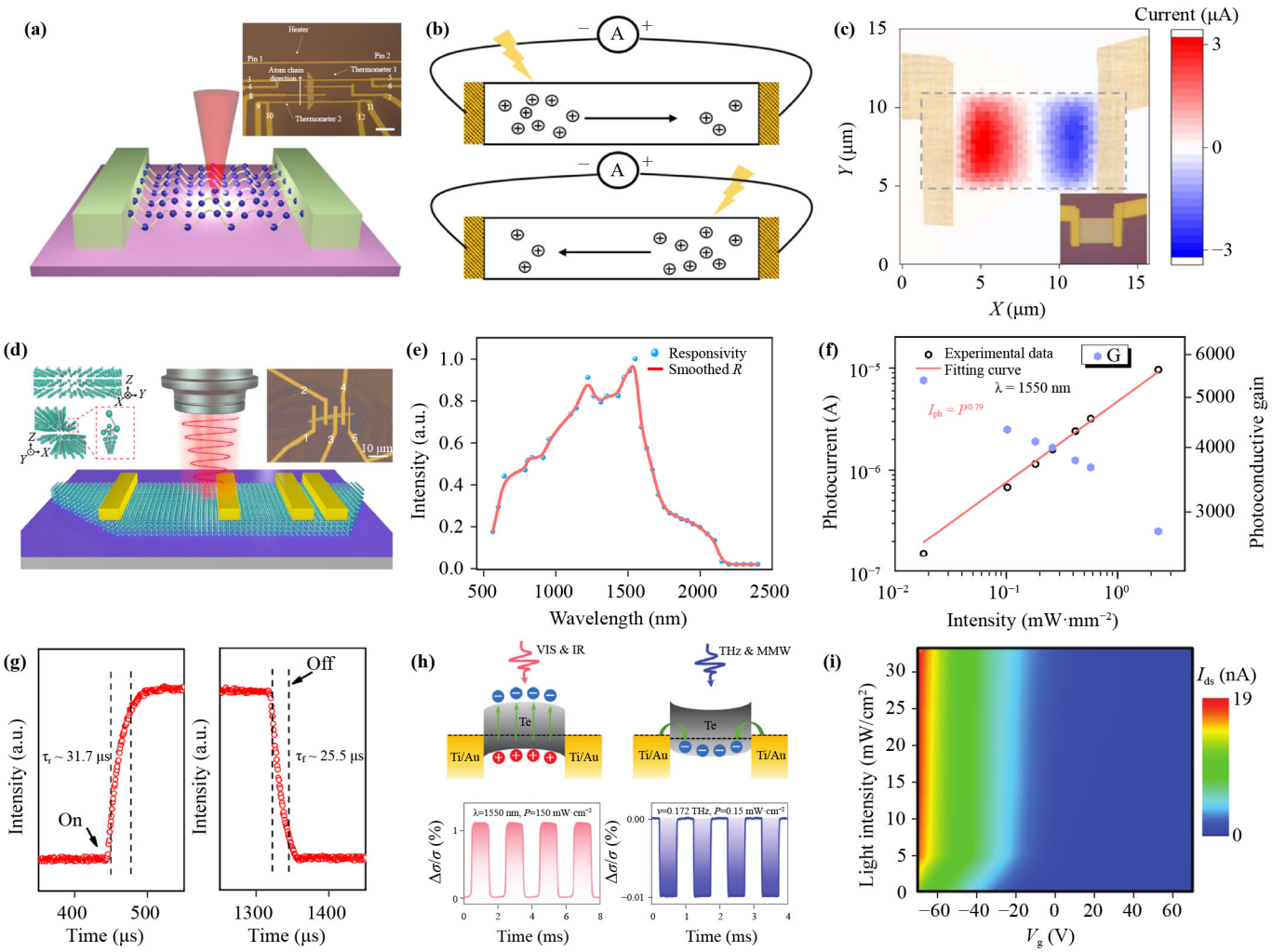

Fig. 8 **(a)** Schematic diagram of the Te-based photodetector, where two Ni electrodes were used as contact and a 633 nm, He–Ne laser was used to heat up the Te flake locally. Inset: OM image of the device, the scale bar is 10 μm. **(b)** The principle of LITE mapping. **(c)** The LIFE current mapping of the real device. The inset is the optical image of the same device [132]. **(d)** Schematic of the crystal structure of Te with a helical chain formed by three adjacent tellurium Atoms [63]. **(e)** Photoresponse spectrum of Te-based photodetector under 500 to 2500 nm laser illumination with a power intensity of 0.01 mW·mm^{-2} at V_{ds} of 0.1 V. **(f)** Photocurrent and G versus power intensity under 1550 nm laser illumination. **(g)** Time-resolved photoresponse of Te nanowire photodetector under 1550 nm laser illumination [75]. **(h)** The detection mechanism of the Te detector in different bands [130]. **(i)** Contour plots of transfer curves measured at different light intensity in 80 K, V_{ds} = 1 V [107].

than the right. In this regard, the carrier concentration at the left end will also be higher, which creates a density gradient and the diffusion current flows from left to right, as described in Fig. 8(b). Similarly, when the laser spot moves to the right, the thermoelectric current will flip the sign. The thermoelectric current can be observed in the whole channel as in Fig. 8(c) and gradually changes from positive to negative values.

Tong *et al.* [63] reported a 2D Te-based photodetector for polarized infrared (IR) photodetection and imaging as schematically shown in Fig. 8(d). A large anisotropic ratio of Te ensures polarized imaging in a scattering environment, with the degree of linear polarization over 0.8, opening up possibilities for developing next-generation polarized mid-infrared (MIR) imaging technology. Subsequently, the same group prepared the Te-based photodetector with simultaneous action of photogating effect and photoconductive effect [75]. As shown in Fig. 8(e), the Te-based photodetector exhibit a broadband photoresponse from visible (Vis) (500 nm) to MIR (2500 nm), which corresponding will with its narrow bandgap. Moreover, the photocurrent and G are closely dependent on the power intensity [Fig. 8(f)], the G can up to about 5600. The relationship between photocurrent and power intensity could be fitted through a non-linear function, $I_{ph} = cp^k$. The fitting result ($k = 0.79$) implying that the device under laser illumination is affected by the photogating effect, electron–hole generation, trapping and recombination processes. The R and D^* of the photodetector under 1550 nm laser irradiation up to 6650 A/W and 1.23×10^{12} Jones, respectively. Moreover, the rise and fall times of the photodetector are 31.7 and

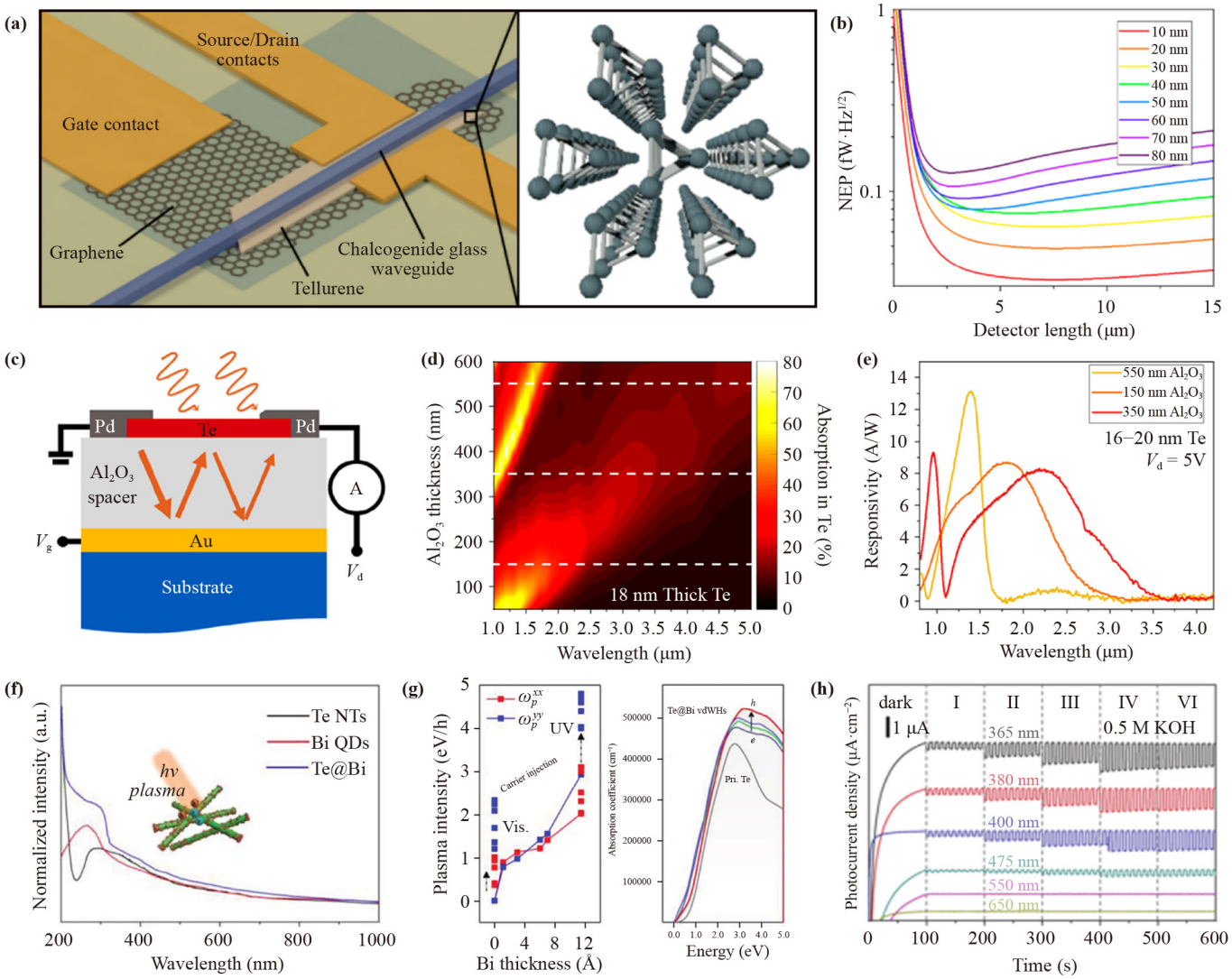

Fig. 9 **(a)** Schematic diagram of the waveguide-integrated Te photodetector. Inset: View of the Te crystal structure along the [0001] axis. **(b)** NEP of the detector as a function of device channel length and Te thickness [134]. **(c)** Schematic diagram of the structure of the optical cavity-coupled 2D Te SWIR photoconductor. **(d)** Absorption of the Te layer with fixed thickness of 18 nm as a function of wavelength and Al_2O_3 thickness. **(e)** R of 2D Te coupled with optical cavities with different Al_2O_3 thicknesses [71]. **(f)** UV-Vis-NIR absorption spectra of Te nanotubes, Bi QDs and Te/Bi heterostructure. **(g)** Plasma intensity of Te/Bi heterostructure with different Bi thickness and carrier doping levels (left) and absorption spectra of pure Te and Te/Bi heterostructure (right). **(h)** Photoresponse of the Te/Bi heterostructure photodetector under different wavelength light illumination in 0.5 M KOH aqueous solution at $V_{ds} = 0$ V [139].

25.5 μs, respectively [Fig. 8(g)], which is one of the fastest speeds among the photoconductive IR detectors. Ma *et al.* [130] further extended the photoresponse of Te-based photodetector to millimeter wavelengths, and found that the photocurrent generation at Vis and IR bands is owing to the photoconductive mechanism, while that at terahertz and millimeter wavelengths is attributed to the electromagnetic trap effect. A positive photoconductance is observed in the Vis and IR bands, while negative photoconductance is observed in the terahertz and millimeter wave bands [Fig. 8(h)]. Moreover, Zhang *et al.* [107] found that the Te-based photodetector exhibit a better gate-dependent photoresponse as shown in Fig. 8(i).

To sum up, Te-based photodetectors have demonstrated ultra-high R, wide response band, fast response speed and diverse physical mechanisms. The photodetection performance can be further improved by enhancing the light–matter interaction and constructing vdWHs as discussed below.

4.3 Tellurium-based photodetector with enhanced light–matter interactions

Integrating 2D Te with nano-optical structures is considered to be an effective way to enhance the light absorption

of Te and thus improve the performance of Te-based photodetectors. 2D Te crystal has naturally passivated surfaces without suspended bonds, and the vdW interactions replacing covalent bonds in the out-of-plane direction. This structure feature allows 2D Te easily integrate with various photonic structures, such as waveguides, optical microcavities and surface plasmons, which is beneficial to further improve its photodetection performance.

Optical waveguides are used to enhance the light absorption of 2D materials by increasing the interaction distance with the swift waves propagating along the waveguide [133]. As shown in Fig. 9(a), Deckoff–Jones *et al.* [134] designed a Te-based photodetector integrated with chalcogenide glass waveguides via theoretical simulation. They found that the waveguide integration extends the spectral range of Te to the MIR, and the signal-to-noise ratio is improved by four orders of magnitude as shown in Fig. 9(b). The NEP values are much higher than the best values previously reported for integrated detectors in MIR waveguides. Hence, the integration of Te crystal with waveguide strategy provides an opportunity to build high-performance integrated MIR photodetectors. We think it would be realized in future experiments as the chalcogenide glass could be deposited directly on 2D materials crystal at room temperature and designed into patterns for using as wave-guiding media [135]. Moreover, Amani *et al.* [71] used an optical cavity substrate consisting of Au/Al_2O_3 to limit the incident light to a small volume by circulating the resonant light inside it, thereby significantly increasing the absorption of Te and realizing a high-performance short wave infrared (SWIR) photodetector. The device structure is shown in Fig. 9(c), where Te with thickness range from 16–20 nm as the channel, and an optical cavity consisting of a thick Au film (100 nm) and an Al_2O_3 dielectric spacer layer is utilized to enhance the absorption. The simulated optical absorption of Te as a function of wavelength and Al_2O_3 thickness [Fig. 9(d)] suggests that the absorption peak can be tuned over a wide spectrum range by adjusting the thickness of Al_2O_3 cavity. As shown in Fig. 9(e), the cutoff wavelength of the Te photodetector can be tuned to 3.4 μm, fully capturing

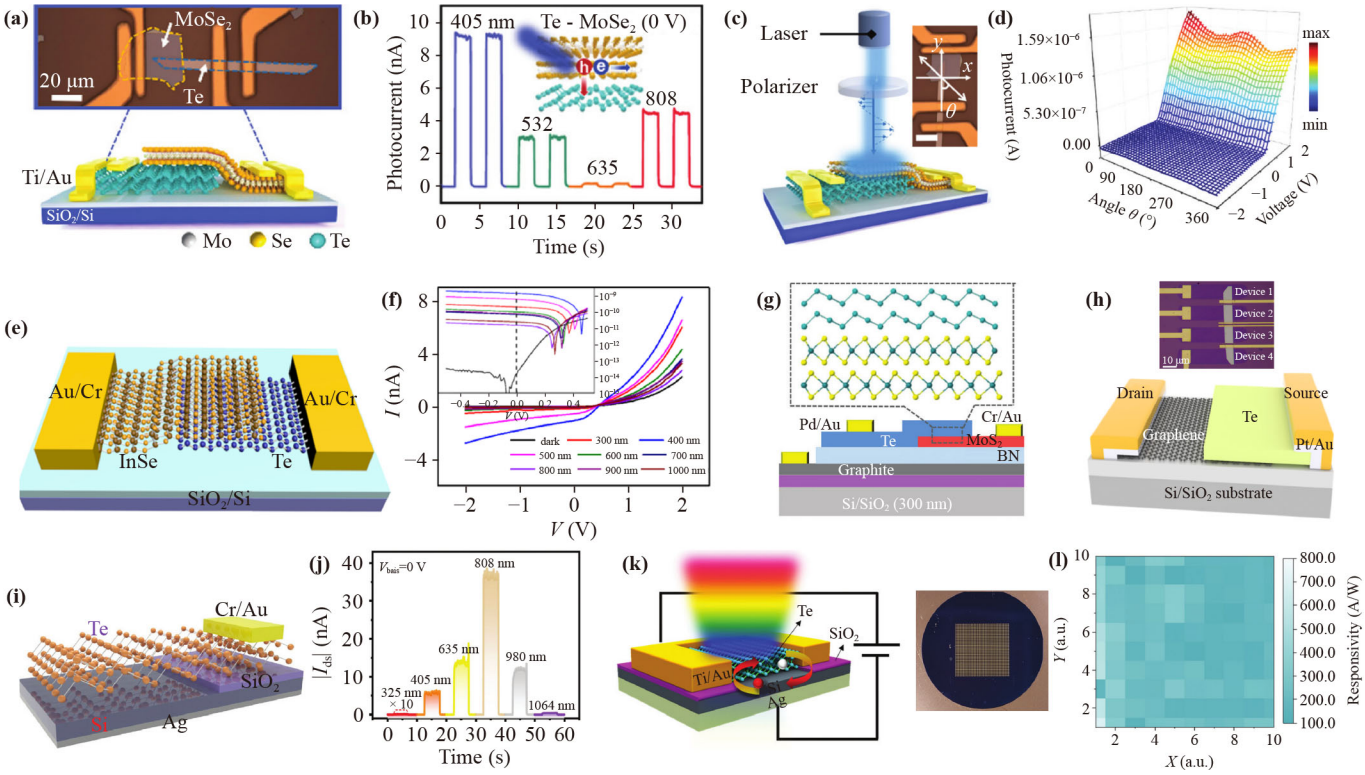

Fig. 10 **(a)** Schematic diagram of the structure and optical image of $Te/MoSe_2$ vdWH photodetector. **(b)** Photoresponse of $Te/MoSe_2$ device under different wavelength illumination. Inset: Schematic diagram of the separation prosses of photogenerated carries at the interface of $Te/MoSe_2$ heterojunction. **(c)** Schematic diagram of polarization-sensitive $Te/MoSe_2$ vdWH photodetector. **(d)** The polarized photocurrent of $Te/MoSe_2$ device for the wavelength of 405 nm at room temperature [140]. **(e)** Schematic diagram of the structure of Te/InSe vdWH photodetector. **(f)** *I*–*V* curves of Te/InSe vdWH photodetector illuminated by light with wavelength from 300–1000 nm [98]. **(g)** Schematic of the structure of the Te/MoS_2 vdWH photodetector [141]. **(h)** Schematic of the structure of the Te/graphene vdWH photodetector [142]. **(i)** Schematic of the structure of the Te/Si vdWH photodetector. **(j)** Photoresponse of Te/Si vdWH photodetector under different wavelength light illumination [146]. **(k)** Schematic diagram of a Te/Si vdWH photodetector and digital photograph of a device matrix with 35 × 35 photodetectors. **(l)** Spatial distribution of the corresponding responsivity of Te/Si vdWH photodetector [113].

the SWIR band.

Plasma excitation enhancement is another route to enhance the light absorption of semiconductor, and it has been widely utilized to elevate the performance of 2D materials-based photodetector [136–138]. Zhang *et al.* [139] prepared a Te-based photodetector by coating metallic Bi quantum dots (QDs) on Te nanotubes, where the electromagnetic waves induced by Bi QDs can enhance the light absorption of Te. Figure 9(f) shows the UV-Vis-NIR absorption spectrum of the Te@Bi photodetector, the optical absorption at the UV region (200–400 nm) is significantly enhanced. DFT calculations show that the plasma intensity increases with the Bi QDs thickness increase, as thicker Bi structure leads to stronger metallic character [left side of Fig. 9(g)]. In comparison with the pristine Te, the absorption of Te@Bi heterojunction in UV region can be significantly increased by carrier injection [right side of Fig. 9(g)], especially for the hole injection situation. As a result, the Te@Bi heterojunction photodetector shows prominent photoresponse with high stability at the UV region [Fig. 9(h)].

4.4 Tellurium-based vdW heterostructure photodetectors

As demonstrated above, the high carrier mobility and wide-tunable bandgap make Te exhibit great potential in photodetection application. However, the high carrier mobility, large carrier density and relative weak absorption of Te lead to Te-based photodetectors suffer from the large dark-current and low D^*, which are innate problems of photoconductive detector. Recently, researchers have devoted to the development of Te-based vdWHs with distinct mechanism by integrating 2D or 1D Te with other 2D materials for achieving high-performance photodetection and more attractive new features.

4.4.1 2D Te-based vdW heterostructure photodetectors

In recent years, a series of 2D Te-based vdWH photodetectors have been reported. Zhao *et al.* [140] proposed a novel polarization-sensitive self-powered imaging photodetector with high performance based on a Te/$MoSe_2$ vdWH [Fig. 10(a)]. Thanks to the strong built-in electric field brought by energy band alignment, the device shows a high rectification ratio of 10^4, indicating a photovoltaic effect. Figure 10(b) shows the self-powered character of the device at different wavelength, the photocurrent can change immediately with better stability when the light switched between on and off. Especially, an ultra-high photocurrent switching ratio of 10^5 can be achieved under a relatively weak light intensity at the wavelength of 405 nm. The photodetector exhibits obvious polarization-sensitive, the anisotropy ratio of photocurrent can reach as high as 16.39 [Figs. 10(c and d)]. Besides, InSe/Te vdWH photodetector was also fabricated [Fig. 10(e)], forming a typical type-II band alignment. The built-in electric field directed from InSe to Te, which enables a record high forward rectification ratio greater than 10^7 [98]. The device shows a broadband photoresponse from 300 to 1000 nm [Fig. 10(f)], and the on-off ratio of photocurrent exceeds 10^4 under Vis light (400 nm) illumination. Yao *et al.* [141] reported a high-performance type-I Te/MoS_2 vdWH photodetector [Fig. 10(g)]. The device selects Pd with high work function as Te contact electrode to reduce the Schottky barrier height and thus improve the hole transport, Cr is used to form ohmic contact with MoS_2, and h-BN dielectric with dangling bondless surface as substrate to reduce the scattering of Te/MoS_2 heterojunction. As results, the device exhibits well-behaved FET properties with a high on/off ratio of 10^7 and a steep subthreshold swing of 150 mV·dec^{-1}, as well as obvious photoresponse during the whole SWIR region (980–3000 nm). Peng *et al.* [142] constructed a Te/graphene vdWH photodetector, achieving a fast response time (28 μs) and broadband photoresponse from Vis to MIR (637–3808 nm) [Fig. 10(i)]. Specifically, the device can be used for room temperature blackbody detection with peak-detection-rate up to 3.69×10^8 Jones.

Besides above all-2D heterojunctions, the dangling-bond-free surfaces of 2D materials also enable vdW interaction with different dimensional materials, forming mixed-dimensional vdWH [143–145]. As shown in Fig. 10(i), a p–n photodiode based on 2D Te and 3D Si mixed-dimensional vdWH with type-I band alignment was constructed [146]. The device exhibits a broadband photoresponse from UV (325 nm) to NIR (1064 nm) and achieves the largest photoresponse at 808 nm light irradiation [Fig. 10(j)]. In particular, the detector exhibits excellent self-powered performance with an ultra-low dark current of only 2 pA and an ultra-high I_{light}/I_{dark} ratio of over 10^5. Lu *et al.* [113] constructed large-scale Te/Si 2D/3D heterojunction arrays by using high-quality centimeter-scale Te nanofilms by pulsed laser deposition [Fig. 10(k)]. The average R, EQE and D^* of the Te/Si vdWH photodetector reach 249 A/W, 76350% and 1.15×10^{11} Jones, respectively. In addition, the large-scale device arrays exhibited similar performance with 100% productivity for 100 randomly tested devices as shown in Fig. 10(l). Cao *et al.* [147] investigated tunneling heterojunctions consisting of 2D Te and non-layered In_2S_3. The Te/In_2S_3 vdWH possess a type-II band alignment, and it can be transformed into type-I or type-III band alignment depending on the applied electric field, which allows tunable tunneling of the photoinduced carriers. The device combines the advantage of the high G from the photo-gating effect of In_2S_3 and the fast response (5 ms) of the tunneling heterojunction.

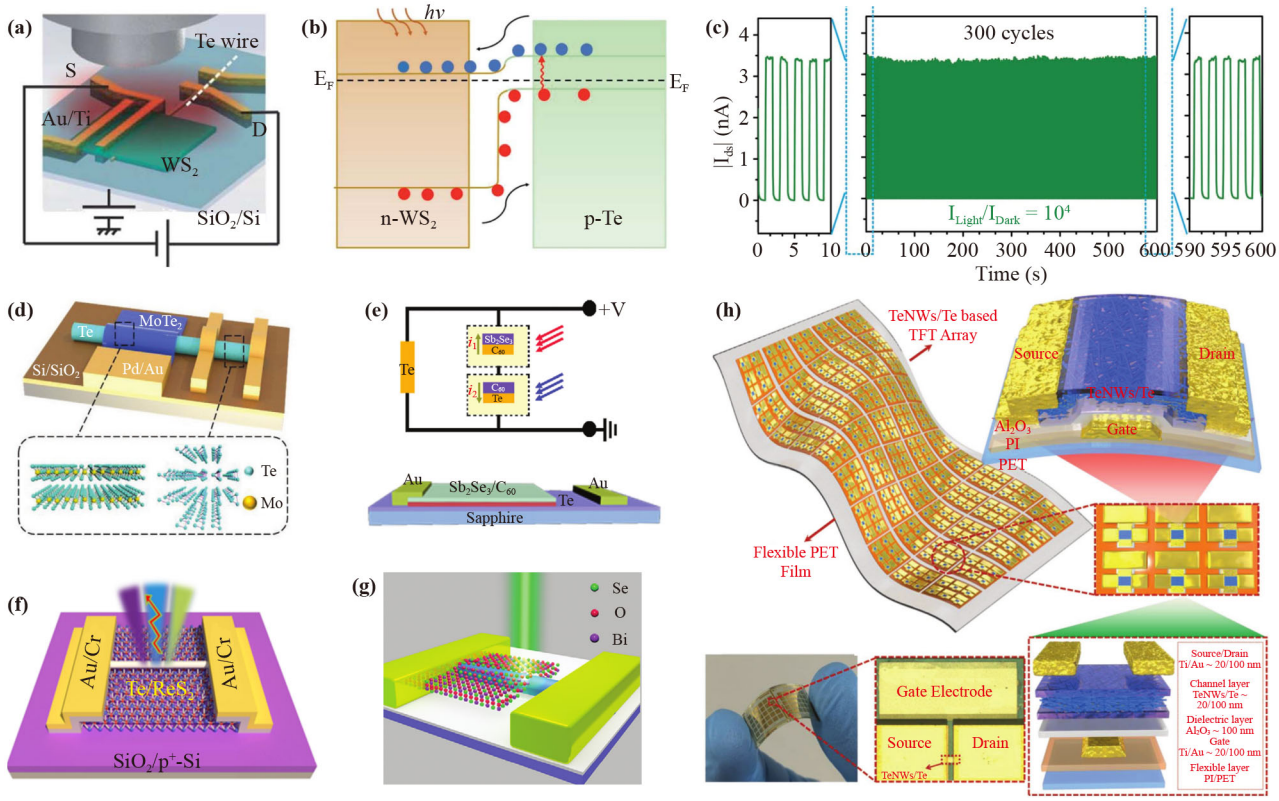

Fig. 11 **(a)** Schematic diagram of the structure of Te/WS_2 vdWH photodetector. **(b)** Carrier transport dynamic of Te/WS_2 vdWH photodetector under light illumination. **(c)** Photoresponse of Te/WS_2 vdWH photodetector under light on-off switching of 300 cycles [148]. **(d)** Schematic diagram of the structure of Te/$MoTe_2$ vdWH photodetector. Inset: Atomic structure of $MoTe_2$ and Te crystals [151]. **(e)** Schematic diagram of the structure of the Te/C_{60}/Sb_2Se_3 photodetector [152]. **(f)** Schematic diagram of the structure of the Te/ReS_2 vdWH photodetector [149]. **(g)** Schematic diagram of the structure of the Te/Bi_2O_2Se vdWH device [150]. **(h)** Schematic diagram of a flexible hybrid structure of Te nanowires/Te film based photodiode device arrays, the zoomed-in images show a single FET device and a 3D section of a single flexible FET device with device layer labels [153].

4.4.2 1D Te-based vdW heterostructure photodetectors

Owing to the quasi-1D structure feature of Te crystal, it can not only form into 2D nanosheets but also easily form into quasi-1D nanowires during its preparation. Hence, many novel Te-based photodetectors with intriguing properties have been constructed by combining 1D Te nanowires with various 2D materials. Han *et al.* constructed a mix-dimensional vertical vdWH by transferring mechanically exfoliated 2D WS_2 nanosheets on epitaxially grown 1D Te [Fig. 11(a)] [148]. The photogenerated carrier transport process of Te/WS_2 heterojunction under light illumination is schematically shown in Fig. 11(b), where a type-II energy band alignment is formed. The separation of photogenerated electron-hole pairs in the depletion region of WS_2 and Te interface driven by the built-in electric field forms the photocurrent. Notably, the photocurrent generation mechanism of most Te-based vdWH photodetectors is analogous. As shown in Fig. 11(c), the photoresponse of the photodetector shows negligible degradation after 300 cycles of light on-off switching, indicating an excellent stability. Tao *et al.* [149] proposed a mixed dimensional vdWH of 1D Te and 2D ReS_2 [Fig. 11(d)]. The type-II heterojunction can improve the injection and separation efficiency of photoexcited electron-hole pairs. So, the heterojunction device has both ultrafast optical response (5 ms) and high R (180 A/W). Furthermore, the 1D Te and 2D Bi_2O_2Se heterodiode with type-II band alignment [Fig. 11(e)] achieved a high rectification ratio of 3.6×10^4, especially they obtained a super-linearity photoelectric conversion phenomenon that can be explained by a super-linearity model based on an intra-gap trap-assisted complex [150].

Recently, several studies have endeavored to improve the applicability of Te-based photodetectors by modifying materials, substrates, or depositing charge-regulation medium. For example, Zhao *et al.* [151] selected the bipolar 2D $MoTe_2$ to construct heterojunctions with 1D Te nanowires [Fig. 11(f)]. Due to the bipolar nature of $MoTe_2$, forward rectifying and reverse rectifying characteristics can be achieved by applying different gate voltages. As a result, the device shows distinct gate-tunable photoresponse at positive and negative gate voltages.

Table 1 Performance of Te-based photodetectors.

Device	Responsivity (A/W)	Detectivity (Jones)	On/off ratio	Response time	Spectral range (nm)	Refs.
2D Te	15	1.24×10^{8}	10^{4}	/	532 nm	[107]
2D Te	986	1.19×10^{10}	/	2.5 μs	Vis to millimeter wave	[130]
2D Te	2.53	4.68×10^{8}	/			[75]
1D Te	6650	1.23×10^{12}	/	25.5 μs	500–2500 nm	[75]
2D Te/$MoSe_2$	2106	2.91×10^{13}	10^{5}	22 ms	405–808 nm	[140]
2D Te/InSe	0.45	10^{13}	10^{4}	600 μs	300–1000 nm	[98]
2D Te/MoS_2	28.4	2.7×10^{10}	10^{7}	/	980–3000 nm	[141]
2D Te/Gra	0.0964	1.04×10^{9}	10^{3}	28 μs	Vis to MIR	[142]
2D Te/In_2S_3	146	2.1×10^{11}	10^{5}	3 ms	405–808 nm	[147]
2D Te/Si	6.49	7.79×10^{12}	10^{5}	26 ms	325–1064 nm	[146]
2D Te/Si	249	1.15×10^{11}	10^{8}	4.4 ms	370.6–2240 nm	[113]
1D Te/WS_2	471	1.24×10^{12}	52	14.7 ms	400–750 nm	[148]
1D Te/$MoTe_2$	3.0×10^{4}	4.9×10^{11}	/	4.8 ms	520, 940, 1310 nm	[151]
1D Te/Sb_2Se_3	110.8	10^{10}-10^{13}	/	31 ms	405–4500 nm	[152]
1D Te/ReS_2	180	7.2×10^{9}	10^{3}	5 ms	Vis	[149]
1DTe/Bi_2O_2Se	130	2.5×10^{11}	10^{4}	330 μs	405, 532, 635 nm	[150]
1D Te/2D Te	30	5.11×10^{11}	10^{4}	2.37 s	405, 532, 638 nm	[153]

Zhang *et al.* [152] fabricated a Te/Sb_2Se_3 vdWH photodetector as shown in Fig. 11(g). By depositing C_{60} between Te and Sb_2Se_3 as the charge regulation medium, a novel binary photocurrent signal output phenomenon depending on wavelengths and optical power densities is observed. These works provide a new pathway to fabricate multifunctional Te-based optoelectronic device, indicating Te-based vdWH devices are expected to utilized in next-generation broadband optoelectronic devices with light-controlled logic signal recognition function. Moreover, large-area flexible Te-based FET device arrays were constructed via depositing 1D Te nanowires and 2D Te films on a flexible substrate to form the mix-dimensional heterostructure [153]. These devices show stable and uniform electrical, optical, and photoelectrical properties, exhibiting great potential of Te in large-scale flexible optoelectronic device applications.

In summary, constructing Te-based vdWH is an effective way to improve the photodetection performance such as D^* and response rate. Especially, the mixed-dimensional vdWH provides more degree of freedom to the selection of materials and thus can compensate for the intrinsic weakness of 2D Te crystals to realize their full potential. Moreover, compared with photoconductive Te photodetectors, Te-based vdWH photodiodes have a built-in electric field, which helps to separate and collect photogenerated carriers to shorten the response time of the detector. To facilitate a clear comparison, the figures-of-merit for Te-based photodetectors are listed in Table 1.

5 Conclusion and perspectives

Within just a few years, there has been a rapid surge of interest and tremendous progress for the attractive single-element 2D Te material. Besides the communal properties similar to other 2D materials, the unusual chiral helical-chain structure of Te endows them abundant exciting physicochemical properties, such as wide-tunable bandgap, high carrier mobility and inherent strong anisotropy. As a result, it has been shown to have potential for a wide range of important applications including FET, inverter, broadband polarization-sensitive photodetector, and photodiode. Despite it has achieved considerable research progresses and been revealed extraordinary application potential, the research about 2D Te is still in its infancy stage, and many challenges and opportunities about its property, preparation and device application deserve to be further explored. There are mainly include the following aspects.

5.1 Property

Since the first preparation of 2D Te, a series of excellent properties have been discovered. For example, 2D Te possess a scare p-type conduction feature and an ultrahigh carrier mobility (thousands of $cm^2{\cdot}V^{-1}{\cdot}s^{-1}$), which make it an ideal candidate for constructing high-performance FETs and logic devices. The strong light-matter interaction together with the wide tunable bandgap of 2D Te are highly desired for building broadband optoelectronic devices. The low crystal symmetry of Te makes it an anisotropic 2D material which exhibits strong anisotropic electrical, optical, vibrational, thermal, and magnetic properties. These unique properties of Te open up excellent potential for designing conceptually new devices where the strong anisotropic properties are required. Certainly, the anisotropy ratio of Te needs to be further enhanced to fulfill the real applications, which

could be realized by applying strain or coupling with the anisotropic plasma nanostructures. Especially, the unusual chiral helical-chain structure reflects a unique feature of Weyl cones and can support helicity-dependent photocurrent generation, providing significant opportunities for exploring the novel chirality-related optical, electrical, and chemical properties in the 2D system. Moreover, the flexible mechanical properties and heavy atomic mass in 2D Te led to a large in-plane piezoelectric coefficient and excellent thermoelectric properties, which provides more choices for physical properties research.

5.2 Preparation

Large-scale, high-quality 2D Te materials with different morphologies have been prepared by various methods, including solution synthesis, LPE, CVD, and PVD, which promotes the development of Te-based electronic and optoelectronic device applications. However, the preparation of 2D Te to satisfy the high-performance device application still faces many problems and challenges. For example, most of 2D Te crystals used in presently reported devices are prepared by the solution synthesis method which usually led to the low crystal quality of Te. In contrast, vapor phase deposition growth can prepare high-quality 2D Te in large-scale, but it is difficult to control the morphology, thickness, and crystal face. Just like a coin with two sides, the quasi-1D vdW structure feature of Te endow it many novel properties, but that also make Te easily grown into 1D nanowire, and the obtained 2D Te has several different crystal faces. To date, it is still lacking a controllable way to selective obtain 1D or 2D Te with specified crystal face. Hence, it is necessary to further develop effective vapor deposition growth strategies to realize the morphology, thickness, and crystal face controllable preparation of Te crystals. Moreover, the strong anisotropy of 2D Te makes its large-scale device applications have higher requirements for the lattice orientation than that of other isotropy 2D materials, as the random orientations of Te grains prepared via present approaches inevitably bring heterogeneous properties. Hence, developing effective approaches to synthesize large-scale 2D Te with uniform orientation and controllable thickness is highly desired, and that should be the primary task in future research work. Furthermore, we suggest that more theory simulation about Te crystal growth should be emphasized, which could guide its controllable synthesis. We believe, once the above goals are achieved, the fundamental properties and device performances of CVD-grown Te would have huge room to be further improved.

The quasi-1D vdW structure and the distinctive properties of 2D Te offer both opportunities and challenges for the integration of them with other 2D TMDs materials to build many novel low-dimensional nanostructures for engineering their interface structures, energy band structures, properties, and device applications. Though initially progresses have been achieved in all above aspects, they are far away from the expectations, and thus further in-depth studies are required. All in all, controlled preparation is the key that determines the future of Te.

5.3 Device application

Thanks to the superior properties and the successful preparation of 2D Te, its electronic and optoelectronic device applications have gottem a booming development in recent years, a series of Te-based devices have been fabricated such as FETs, photodetectors, and photodiodes. It was found that the 2D Te-based FET show outstanding performance compared with other 2D TMDs in terms of the carrier mobility and on-off ratio, and the 2D Te-based photodetectors superior performance such as high R, broadband response, especially the ability to detect polarized light. To further improve the performance of 2D Te-based devices, h-BN encapsulation, 2D semi metallic materials as contact electrodes and nano-optical structures integration were developed. Though great progresses have been achieved on the 2D Te-based electronic and optoelectronic devices, these researches are still in the preliminary stage of exploration.

For the Te-based FET, the performance still has great room to be further enhanced by optimizing the channel length, electrode contacts as well as the dielectric layer. In addition, combining the p-type 2D Te with the other n-type 2D TMDs could build tunable multivalue logic inverters. For the Te-based photodetector, present studies are mainly focused on the Vis to NIR band, the development of ultra -broadband (UV to terahertz band) devices is highly preferred. An in-depth understanding of the photocurrent generation and carrier recombination mechanisms of Te-based photodetector is needed for further improving the performance. The anisotropic ratio of Te-based polarization-sensitive photodetector is relative larger that of most of anisotropic 2D TMDs, but it still has a large gap to the reality application. We think there are several possible strategies can improve the anisotropic ratio: i) construct vdWH; ii) integrate with anisotropic plasma nanostructures, iii) apply uniaxial strain. The novel chirality-related optical and electronic properties are also directly applicable of Te to helicity-sensitive optoelectronics devices to detect circular-polarization optical. Moreover, 2D Te-based vdWH photodetectors are formed mostly by type-II energy band alignment, and the physical mechanism is mainly the photovoltaic effect. So, it is necessary to explore Te-based vdWH photodetectors with new device structures, diverse band alignments and physical mechanisms in future research. 2D Te can be easily integrated with on-chip structures, such as waveguides, photonic crystals,

and metasurfaces, to further enhance optoelectronic responses, which is worth more investigation. Finally, the exploration of 2D Te in photothermal devices and blackbody detection devices are still deficient, it is necessary to further explore the mechanism and optimize the device structure to enhance their performance.

In a word, the above features that enable 2D Te to be unique and deserve to be studied in depth. Herein, Te is just a more general representation of group-VIA single-element 2D crystals or those similarly low-symmetry single-element 2D materials. We believe that this review article will promote the exploration of 2D materials and accelerate the development of materials science.

Acknowledgements This work was supported by the National Natural Science Foundation of China (Nos. 22222505 and 51972204), the Natural Science Basic Research Plan in Shaanxi Province (Nos. 2021JM316 and 2021JM-203), the Science and Technology Program of Shaanxi Province (No. 2017KJXX-16), the Shaanxi Sanqin Scholars Innovation Team, the Fundamental Innovation Project and Young Scientist Initiative Project in School of Materials Science and Engineering (SNNU).

References

1. K. S. Novoselov, A. K. Geim, S. V. Morozov, D. Jiang, Y. Zhang, S. V. Dubonos, I. V. Grigorieva, and A. A. Firsov, Electric field effect in atomically thin carbon films, *Science* 306(5696), 666 (2004)
2. C. Tan, X. Cao, X. J. Wu, Q. He, J. Yang, X. Zhang, J. Chen, W. Zhao, S. Han, G. H. Nam, M. Sindoro, and H. Zhang, Recent advances in ultrathin two-dimensional nanomaterials, *Chem. Rev.* 117(9), 6225 (2017)
3. H. Zhang, Ultrathin two-dimensional nanomaterials, *ACS Nano* 9(10), 9451 (2015)
4. D. Akinwande, C. Huyghebaert, C. H. Wang, M. I. Serna, S. Goossens, L. J. Li, H. S. P. Wong, and F. H. L. Koppens, Graphene and two-dimensional materials for silicon technology, *Nature* 573(7775), 507 (2019)
5. A. J. Mannix, X. F. Zhou, B. Kiraly, J. D. Wood, D. Alducin, B. D. Myers, X. Liu, B. L. Fisher, U. Santiago, J. R. Guest, M. J. Yacaman, A. Ponce, A. R. Oganov, M. C. Hersam, and N. P. Guisinger, Synthesis of borophenes: Anisotropic, two-dimensional boron polymorphs, *Science* 350(6267), 1513 (2015)
6. W. Zhai, T. Xiong, Z. K. He, S. Lu, Z. Lai, Q. He, C. Tan, and H. Zhang, Nanodots derived from layered materials: Synthesis and applications, *Adv. Mater.* 33(46), 2006661 (2021)
7. Y. Xiao, M. Zhou, J. Liu, J. Xu, and L. Fu, Phase engineering of two-dimensional transition metal dichalcogenides, *Sci. China Mater.* 62(6), 759 (2019)
8. T. Chowdhury, E. C. Sadler, and T. J. Kempa, Progress and prospects in transition-metal dichalcogenide research beyond 2D, *Chem. Rev.* 120(22), 12563 (2020)
9. S. Roy, X. Zhang, A. B. Puthirath, A. Meiyazhagan, S. Bhattacharyya, et al., Structure, properties and applications of two-dimensional hexagonal boron nitride, *Adv. Mater.* 33(44), 2101589 (2021)
10. Y. Cao, V. Fatemi, S. Fang, K. Watanabe, T. Taniguchi, E. Kaxiras, and P. Jarillo-Herrero, Unconventional superconductivity in magic-angle graphene superlattices, *Nature* 556(7699), 43 (2018)
11. H. Zhao, C. W. Zhang, W. X. Ji, R. W. Zhang, S. S. Li, S. S. Yan, B. M. Zhang, P. Li, and P. J. Wang, Unexpected giant-gap quantum spin hall insulator in chemically decorated plumbene monolayer, *Sci. Rep.* 6(1), 20152 (2016)
12. S. B. Lu, L. L. Miao, Z. N. Guo, X. Qi, C. J. Zhao, H. Zhang, S. C. Wen, D. Y. Tang, and D. Y. Fan, Broadband nonlinear optical response in multi-layer black phosphorus: An emerging infrared and mid-infrared optical material, *Opt. Express* 23(9), 11183 (2015)
13. K. S. Novoselov, D. V. Andreeva, W. Ren, and G. Shan, Graphene and other two-dimensional materials, *Front. Phys.* 14(1), 13301 (2019)
14. M. Chhowalla, D. Jena, and H. Zhang, Two-dimensional semiconductors for transistors, *Nat. Rev. Mater.* 1(11), 16052 (2016)
15. Y. Liu, X. Duan, H. J. Shin, S. Park, Y. Huang, and X. Duan, Promises and prospects of two-dimensional transistors, *Nature* 591(7848), 43 (2021)
16. C. Hu, Finfet and UTB - how to make very short channel MOSFETs, *ECS Trans.* 50(9), 17 (2013)
17. C. Chen, X. Chen, C. Wu, X. Wang, Y. Ping, X. Wei, X. Zhou, J. Lu, L. Zhu, J. Zhou, T. Zhai, J. Han, and H. Xu, Air-stable 2D Cr_5Te_8 nanosheets with thickness-tunable ferromagnetism, *Adv. Mater.* 34(2), 2107512 (2022)
18. C. Zhao, C. Tan, D. H. Lien, X. Song, M. Amani, M. Hettick, H. Y. Y. Nyein, Z. Yuan, L. Li, M. C. Scott, and A. Javey, Evaporated tellurium thin films for p-type field-effect transistors and circuits, *Nat. Nanotechnol.* 15(1), 53 (2020)
19. V. B. Koman, P. Liu, D. Kozawa, A. T. Liu, A. L. Cottrill, Y. Son, J. A. Lebron, and M. S. Strano, Colloidal nanoelectronic state machines based on 2D materials for aerosolizable electronics, *Nat. Nanotechnol.* 13(9), 819 (2018)
20. K. F. Mak, and J. Shan, Photonics and optoelectronics of 2D semiconductor transition metal dichalcogenides, *Nat. Photonics* 10(4), 216 (2016)
21. Z. Cheng, R. Cao, K. Wei, Y. Yao, X. Liu, J. Kang, J. Dong, Z. Shi, H. Zhang, and X. Zhang, 2D materials enabled next-generation integrated optoelectronics: From fabrication to applications, *Adv. Sci. (Weinh.)* 8(11), 2003834 (2021)
22. C. Tan, Z. Luo, A. Chaturvedi, Y. Cai, Y. Du, Y. Gong, Y. Huang, Z. Lai, X. Zhang, L. Zheng, X. Qi, M. H. Goh, J. Wang, S. Han, X. J. Wu, L. Gu, C. Kloc, and H. Zhang, Preparation of high-percentage 1T′-phase transition metal dichalcogenide nanodots for electrochemical hydrogen evolution, *Adv. Mater.* 30(9), 1705509 (2018)
23. X. Chia and M. Pumera, Characteristics and performance of two-dimensional materials for electrocatalysis, *Nat. Catal.* 1(12), 909 (2018)
24. E. Pomerantseva and Y. Gogotsi, Two-dimensional

heterostructures for energy storage, *Nat. Energy* 2(7), 17089 (2017)
25. S. Das, D. Pandey, J. Thomas, and T. Roy, The role of graphene and other 2D materials in solar photovoltaics, *Adv. Mater.* 31(1), 1802722 (2019)
26. K. Kostarelos, Translating graphene and 2D materials into medicine, *Nat. Rev. Mater.* 1(11), 16084 (2016)
27. L. Cheng, X. Wang, F. Gong, T. Liu, and Z. Liu, 2D Nanomaterials for cancer theranostic applications, *Adv. Mater.* 32(13), 1902333 (2020)
28. H. Jiang, L. Zheng, Z. Liu, and X. Wang, Two-dimensional materials: From mechanical properties to flexible mechanical sensors, *InfoMat* 2(6), 1077 (2020)
29. Z. Wang and B. Mi, Environmental applications of 2D molybdenum disulfide (MoS_2) nanosheets, *Environ. Sci. Technol.* 51(15), 8229 (2017)
30. F. H. L. Koppens, T. Mueller, P. Avouris, A. C. Ferrari, M. S. Vitiello, and M. Polini, Photodetectors based on graphene, other two-dimensional materials and hybrid systems, *Nat. Nanotechnol.* 9(10), 780 (2014)
31. Q. X. Qiu and Z. M. Huang, Photodetectors of 2D materials from ultraviolet to terahertz waves, *Adv. Mater.* 33(15), 2008126 (2021)
32. F. W. Zhuge, Z. Zheng, P. Luo, L. Lv, Y. Huang, H. Q. Li, and T. Y. Zhai, Nanostructured materials and architectures for advanced infrared photodetection, *Adv. Mater. Technol.* 2(8), 1700005 (2017)
33. X. H. Li, Y. X. Guo, Y. J. Ren, J. J. Peng, J. S. Liu, C. Wang, and H. Zhang, Narrow-bandgap materials for optoelectronics applications, *Front. Phys.* 17(1), 13304 (2022)
34. M. Cheng, J. B. Yang, X. H. Li, H. Li, R. F. Du, J. P. Shi, and J. He, Improving the device performances of two-dimensional semiconducting transition metal dichalcogenides: Three strategies, *Front. Phys.* 17(6), 63601 (2022)
35. X. Li, C. Chen, Y. Yang, Z. Lei, and H. Xu, 2D Re-based transition metal chalcogenides: Progress, challenges, and opportunities, *Adv. Sci. (Weinh.)* 7(23), 2002320 (2020)
36. Y. Liu, X. D. Duan, Y. Huang, and X. F. Duan, Two-dimensional transistors beyond graphene and TMDCs, *Chem. Soc. Rev.* 47(16), 6388 (2018)
37. R. Cao, H. D. Wang, Z. N. Guo, D. K. Sang, L. Y. Zhang, Q. L. Xiao, Y. P. Zhang, D. Y. Fan, J. Q. Li, and H. Zhang, Black phosphorous/indium selenide photoconductive detector for visible and near-infrared light with high sensitivity, *Adv. Opt. Mater.* 7(12), 1900020 (2019)
38. M. J. Dai, H. Y. Chen, F. K. Wang, M. S. Long, H. M. Shang, Y. X. Hu, W. Li, C. Y. Ge, J. Zhang, T. Y. Zhai, Y. Q. Fu, and P. A. Hu, Ultrafast and sensitive self-powered photodetector featuring self-limited depletion region and fully depleted channel with van der Waals contacts, *ACS Nano* 14(7), 9098 (2020)
39. Y. C. Kim, T. W. Bae, H. J. Kwon, B. I. Kim, and S. H. Ahn, Infrared (IR) image synthesis method of IR real background and modeled IR target, *Infrared Phys. Technol.* 63, 54 (2014)
40. L. J. Pi, P. F. Wang, S. J. Liang, P. Luo, H. Y. Wang, D. Y. Li, Z. X. Li, P. Chen, X. Zhou, F. Miao, and T. Y. Zhai, Broadband convolutional processing using band-alignment-tunable heterostructures, *Nat. Electron.* 5(4), 248 (2022)
41. C. Tan, S. Yin, J. Chen, Y. Lu, W. Wei, H. Du, K. Liu, F. Wang, T. Zhai, and L. Li, Broken-gap PtS_2/WSe_2 van der Waals heterojunction with ultrahigh reverse rectification and fast photoresponse, *ACS Nano* 15(5), 8328 (2021)
42. J. Zheng, Z. Yang, C. Si, Z. Liang, X. Chen, R. Cao, Z. Guo, K. Wang, Y. Zhang, J. Ji, M. Zhang, D. Fan, and H. Zhang, Black phosphorus based all-optical-signal-processing: Toward high performances and enhanced stability, *ACS Photonics* 4(6), 1466 (2017)
43. W. Yang, K. Xin, J. Yang, Q. Xu, C. Shan, and Z. Wei, 2D ultrawide bandgap semiconductors: Odyssey and challenges, *Small Methods* 6(4), 2101348 (2022)
44. J. J. Zha, M. C. Luo, M. Ye, T. Ahmed, X. C. Yu, D. H. Lien, Q. Y. He, D. Y. Lei, J. C. Ho, J. Bullock, K. B. Crozier, and C. L. Tan, Infrared photodetectors based on 2D materials and nanophotonics, *Adv. Funct. Mater.* 32(15), 2111970 (2022)
45. X. Guan, X. Yu, D. Periyanagounder, M. R. Benzigar, J. K. Huang, C. H. Lin, J. Kim, S. Singh, L. Hu, G. Liu, D. Li, J. H. He, F. Yan, Q. J. Wang, and T. Wu, Recent progress in short- to long-wave infrared photodetection using 2D materials and heterostructures, *Adv. Opt. Mater.* 9(4), 2001708 (2021)
46. Y. Yang, K. X. Zhang, L. B. Zhang, G. Hong, C. Chen, H. M. Jing, J. B. Lu, P. Wang, X. S. Chen, L. Wang, and H. Xu, Controllable growth of type-II Dirac semimetal $PtTe_2$ atomic layer on Au substrate for sensitive room temperature terahertz photodetection, *InfoMat* 3(6), 705 (2021)
47. M. Dai, C. Wang, M. Ye, S. Zhu, S. Han, F. Sun, W. Chen, Y. Jin, Y. Chua, and Q. J. Wang, High-performance, polarization-sensitive, long-wave infrared photodetection via photothermoelectric effect with asymmetric van der Waals contacts, *ACS Nano* 16(1), 295 (2022)
48. E. J. Reed, Two-dimensional tellurium, *Nature* 552(7683), 40 (2017)
49. S. H. Yang, Chirality tweaks spins in tellurium, *Nat. Mater.* 21(5), 494 (2022)
50. Y. Wang, G. Qiu, R. Wang, S. Huang, Q. Wang, Y. Liu, Y. Du, W. A. III Goddard, M. J. Kim, X. Xu, P. D. Ye, and W. Wu, Field-effect transistors made from solution-grown two-dimensional tellurene, *Nat. Electron.* 1(4), 228 (2018)
51. C. F. Shen, Y. H. Liu, J. B. Wu, C. Xu, D. Z. Cui, Z. Li, Q. Z. Liu, Y. R. Li, Y. X. Wang, X. Cao, H. Kumazoe, F. Shimojo, A. Krishnamoorthy, R. K. Kalia, A. Nakano, P. D. Vashishta, M. R. Amer, A. N. Abbas, H. Wang, W. Z. Wu, and C. W. Zhou, Tellurene photodetector with high gain and wide bandwidth, *ACS Nano* 14(1), 303 (2020)
52. D. A. Nguyen, Y. Jo, T. U. Tran, M. S. Jeong, H. Kim, and H. Im, Electrically and optically controllable p–n junction memtransistor based on an Al_2O_3 encapsulated 2D Te/ReS_2 van der Waals heterostructure, *Small Methods* 5(12), 2101303 (2021)

53. B. Z. Yan, G. R. Li, B. N. Shi, J. T. Liu, H. K. Nie, K. J. Yang, B. T. Zhang, and J. He, 2D tellurene/black phosphorus heterojunctions based broadband nonlinear saturable absorber, *Nanophotonics* 9(8), 2593 (2020)
54. B. Zheng, Z. Wu, F. Guo, R. Ding, J. Mao, M. Xie, S. P. Lau, and J. Hao, Large-area tellurium/germanium heterojunction grown by molecular beam epitaxy for high-performance self-powered photodetector, *Adv. Opt. Mater.* 9(20), 2101052 (2021)
55. W. Huang, Y. Zhang, Q. You, P. Huang, Y. Wang, Z. N. Huang, Y. Ge, L. Wu, Z. Dong, X. Dai, Y. Xiang, J. Li, X. Zhang, and H. Zhang, Enhanced photodetection properties of tellurium@selenium roll-to-roll nanotube heterojunctions, *Small* 15(23), 1900902 (2019)
56. C. Wang, P. Z. Wang, S. Y. Chen, W. Wen, W. Q. Xiong, Z. Z. Liu, Y. F. Liu, J. Q. He, and Y. S. Wang, Anisotropic properties of tellurium nanoflakes probed by polarized Raman and transient absorption microscopy: Implications for polarization-sensitive applications, *ACS Appl. Nano Mater.* 5(2), 1767 (2022)
57. J. W. Liu, J. H. Zhu, C. L. Zhang, H. W. Liang, and S. H. Yu, Mesostructured assemblies of ultrathin superlong tellurium nanowires and their photoconductivity, *J. Am. Chem. Soc.* 132(26), 8945 (2010)
58. H. Peng, N. Kioussis, and G. J. Snyder, Elemental tellurium as a chiral p-type thermoelectric material, *Phys. Rev. B* 89(19), 195206 (2014)
59. Y. Wang, Y. Wang, Y. Dong, L. Zhou, H. Wei, M. Long, S. Xiao, and J. He, The nonlinear optical transition bleaching in tellurene, *Nanoscale* 13(37), 15882 (2021)
60. J. P. Hermann, G. Quentin, and J. M. Thuillier, Determination of the d_{14} piezoelectric coefficient of tellurium, *Solid State Commun.* 7(1), 161 (1969)
61. C. Lin, W. Cheng, G. Chai, and H. Zhang, Thermoelectric properties of two-dimensional selenene and tellurene from group-VI elements, *Phys. Chem. Chem. Phys.* 20(37), 24250 (2018)
62. W. Zhang, Q. Wu, O. V. Yazyev, H. Weng, Z. Guo, W. D. Cheng, and G. L. Chai, Topological phase transitions driven by strain in monolayer tellurium, *Phys. Rev. B* 98(11), 115411 (2018)
63. L. Tong, X. Y. Huang, P. Wang, L. Ye, M. Peng, L. C. An, Q. D. Sun, Y. Zhang, G. M. Yang, Z. Li, F. Zhong, F. Wang, Y. X. Wang, M. Motlag, W. Z. Wu, G. J. Cheng, and W. D. Hu, Stable mid-infrared polarization imaging based on quasi-2D tellurium at room temperature, *Nat. Commun.* 11(1), 2308 (2020)
64. G. Jnawali, Y. Xiang, S. M. Linser, I. A. Shojaei, R. Wang, G. Qiu, C. Lian, B. M. Wong, W. Wu, P. D. Ye, Y. Leng, H. E. Jackson, and L. M. Smith, Ultrafast photoinduced band splitting and carrier dynamics in chiral tellurium nanosheets, *Nat. Commun.* 11(1), 3991 (2020)
65. W. Wu, G. Qiu, Y. Wang, R. Wang, and P. Ye, Tellurene: Its physical properties, scalable nanomanufacturing, and device applications, *Chem. Soc. Rev.* 47(19), 7203 (2018)
66. Z. Shi, R. Cao, K. Khan, A. K. Tareen, X. Liu, W. Liang, Y. Zhang, C. Ma, Z. Guo, X. Luo, and H. Zhang, Two-dimensional tellurium: Progress, challenges, and prospects, *Nano-Micro Lett.* 12(1), 99 (2020)
67. Z. Yan, H. Yang, Z. Yang, C. Ji, G. Zhang, Y. Tu, G. Du, S. Cai, and S. Lin, Emerging two-dimensional tellurene and tellurides for broadband photodetectors, *Small* 18(20), 2200016 (2022)
68. G. Qiu, A. Charnas, C. Niu, Y. X. Wang, W. Z. Wu, and P. D. Ye, The resurrection of tellurium as an elemental two-dimensional semiconductor, *npj 2D Mater. Appl.* 6(1), 17 (2022)
69. Z. Zhu, X. Cai, S. Yi, J. Chen, Y. Dai, C. Niu, Z. Guo, M. Xie, F. Liu, J. H. Cho, Y. Jia, and Z. Zhang, Multivalency-driven formation of Te-based monolayer materials: A combined first-principles and experimental study, *Phys. Rev. Lett.* 119(10), 106101 (2017)
70. B. Wu, X. Liu, J. Yin, and H. Lee, Bulk β-Te to few layered β-tellurenes: Indirect to direct band-gap transitions showing semiconducting property, *Mater. Res. Express* 4(9), 095902 (2017)
71. M. Amani, C. L. Tan, G. Zhang, C. S. Zhao, J. Bullock, X. H. Song, H. Kim, V. R. Shrestha, Y. Gao, K. B. Crozier, M. Scott, and A. Javey, Solution-synthesized high-mobility tellurium nanoflakes for short-wave infrared photodetectors, *ACS Nano* 12(7), 7253 (2018)
72. Z. He, Y. Yang, J. W. Liu, and S. H. Yu, Emerging tellurium nanostructures: Controllable synthesis and their applications, *Chem. Soc. Rev.* 46(10), 2732 (2017)
73. J. S. Qiao, Y. H. Pan, F. Yang, C. Wang, Y. Chai, and W. Ji, Few-layer tellurium: One-dimensional-like layered elementary semiconductor with striking physical properties, *Sci. Bull. (Beijing)* 63(3), 159 (2018)
74. Y. Y. Liu, W. Z. Wu, and W. A. III Goddard, Tellurium: Fast electrical and atomic transport along the weak interaction direction, *J. Am. Chem. Soc.* 140(2), 550 (2018)
75. M. Peng, R. Z. Xie, Z. Wang, P. Wang, F. Wang, H. N. Ge, Y. Wang, F. Zhong, P. S. Wu, J. F. Ye, Q. Li, L. L. Zhang, X. Ge, Y. Ye, Y. C. Lei, W. Jiang, Z. G. Hu, F. Wu, X. H. Zhou, J. S. Miao, J. L. Wang, H. G. Yan, C. X. Shan, J. N. Dai, C. Q. Chen, X. S. Chen, W. Lu, and W. D. Hu, Blackbody-sensitive room-temperature infrared photodetectors based on low-dimensional tellurium grown by chemical vapor deposition, *Sci. Adv.* 7(16), eabf7358 (2021)
76. X. Han, H. M. Stewart, S. A. Shevlin, C. R. Catlow, and Z. X. Guo, Strain and orientation modulated bandgaps and effective masses of phosphorene nanoribbons, *Nano Lett.* 14(8), 4607 (2014)
77. H. Morgan Stewart, S. A. Shevlin, C. R. A. Catlow, and Z. X. Guo, Compressive straining of bilayer phosphorene leads to extraordinary electron mobility at a new conduction band edge, *Nano Lett.* 15(3), 2006 (2015)
78. S. Zhang, C. Li, Z. Xiao Guo, J. H. Cho, W. S. Su, and Y. Jia, Magnetic evolution and anomalous Wilson transition in diagonal phosphorene nanoribbons driven by strain, *Nanotechnology* 26(29), 295402 (2015)
79. Z. Zhu, C. Cai, C. Niu, C. Wang, Q. Sun, X. Han, Z. Guo and Y. Jia, Tellurene-a monolayer of tellurium from first-principles prediction, arXiv: 1605.03253v1

(2016)
80. Z. L. Zhu, X. L. Cai, S. H. Yi, J. L. Chen, Y. W. Dai, C. Y. Niu, Z. X. Guo, M. H. Xie, F. Liu, J. H. Cho, Y. Jia, and Z. Y. Zhang, Multivalency-driven formation of Te-based monolayer materials: A combined first-principles and experimental study, *Phys. Rev. Lett.* 119(10), 106101 (2017)
81. J. Wang, C. Z. Jiang, W. Q. Li, and X. H. Xiao, Anisotropic low-dimensional materials for polarization-sensitive photodetectors: From materials to devices, *Adv. Opt. Mater.* 10(6), 2102436 (2022)
82. X. Li, H. Y. Liu, C. M. Ke, W. Q. Tang, M. Y. Liu, F. H. Huang, Y. P. Wu, Z. M. Wu, and J. Y. Kang, Review of anisotropic 2D materials: Controlled growth, optical anisotropy modulation, and photonic applications, *Laser Photonics Rev.* 15(12), 2100322 (2021)
83. J. L. Zhao, D. T. Ma, C. Wang, Z. N. Guo, B. Zhang, J. Q. Li, G. H. Nie, N. Xie, and H. Zhang, Recent advances in anisotropic two-dimensional materials and device applications, *Nano Res.* 14(4), 897 (2021)
84. L. D. Xian, A. P. Paz, E. Bianco, P. M. Ajayan and A. Rubio, Square selenene and tellurene: Novel group VI elemental 2D materials with nontrivial topological properties, *2D Mater.* 4(4), 041003 (2017)
85. K. C. Nomura, Optical activity in tellurium, *Phys. Rev. Lett.* 5(11), 500 (1960)
86. V. M. Asnin, A. A. Bakun, A. M. Danishevskii, E. L. Ivchenko, G. E. Pikus, and A. A. Rogachev, "Circular" photogalvanic effect in optically active crystals, *Solid State Commun.* 30(9), 565 (1979)
87. T. Furukawa, Y. Shimokawa, K. Kobayashi, and T. Itou, Observation of current-induced bulk magnetization in elemental tellurium, *Nat. Commun.* 8(1), 954 (2017)
88. F. Calavalle, M. Suárez-Rodríguez, B. Martín-García, A. Johansson, D. C. Vaz, H. Yang, I. V. Maznichenko, S. Ostanin, A. Mateo-Alonso, A. Chuvilin, I. Mertig, M. Gobbi, F. Casanova, and L. E. Hueso, Gate-tuneable and chirality-dependent charge-to-spin conversion in tellurium nanowires, *Nat. Mater.* 21(5), 526 (2022)
89. L. A. Agapito, N. Kioussis, W. A. Goddard, and N. P. Ong, Novel family of chiral-based topological insulators: Elemental tellurium under strain, *Phys. Rev. Lett.* 110(17), 176401 (2013)
90. X. X. Xue, Y. X. Feng, L. Liao, Q. J. Chen, D. Wang, L. M. Tang, and K. Chen, Strain tuning of electronic properties of various dimension elemental tellurium with broken screw symmetry, *J. Phys.: Condens. Matter* 30(12), 125001 (2018)
91. Y. J. Kwack, T. T. T. Can, and W. S. Choi, Bottom-up water-based solution synthesis for a large MoS_2 atomic layer for thin-film transistor applications, *npj 2D Mater. Appl.* 5(1), 84 (2021)
92. M. S. Sokolikova, P. C. Sherrell, P. Palczynski, V. L. Bemmer, and C. Mattevi, Direct solution-phase synthesis of 1T′ WSe_2 nanosheets, *Nat. Commun.* 10(1), 712 (2019)
93. Y. Sun, Y. Wang, D. Sun, B. R. Carvalho, C. G. Read, C. Lee, Z. Lin, K. Fujisawa, J. A. Robinson, V. H. Crespi, M. Terrones, and R. E. Schaak, Low-temperature solution synthesis of few-layer 1T′-$MoTe_2$ nanostructures exhibiting lattice compression, *Angew. Chem. Int. Ed.* 55(8), 2830 (2016)
94. Z. Lu, M. Layani, X. Zhao, L. P. Tan, T. Sun, S. Fan, Q. Yan, S. Magdassi, and H. H. Hng, Fabrication of flexible thermoelectric thin film devices by inkjet printing, *Small* 10(17), 3551 (2014)
95. M. Ding, K. Liang, S. Yu, X. Zhao, H. Ren, B. Zhu, X. Hou, Z. Wang, P. Tan, H. Huang, Z. Zhang, X. Ma, G. Xu, and S. Long, Aqueous-printed Ga_2O_3 films for high-performance flexible and heat-resistant deep ultraviolet photodetector and array, *Adv. Opt. Mater.* 10(16), 2200512 (2022)
96. Y. Dong, Y. Zou, J. Song, J. Li, B. Han, Q. Shan, L. Xu, J. Xue, and H. Zeng, An all-inkjet-printed flexible UV photodetector, *Nanoscale* 9(25), 8580 (2017)
97. J. R. Yao, F. F. Chen, J. J. Li, J. L. Du, D. Wu, Y. T. Tian, C. Zhang, X. J. Li, and P. Lin, Mixed-dimensional Te/CdS van der Waals heterojunction for self-powered broadband photodetector, *Nanotechnology* 32(41), 415201 (2021)
98. F. L. Qin, F. Gao, M. J. Dai, Y. X. Hu, M. M. Yu, L. F. Wang, W. Feng, B. Li, and P. A. Hu, Multilayer InSe–Te van der Waals heterostructures with an ultrahigh rectification ratio and ultrasensitive photoresponse, *ACS Appl. Mater. Interfaces* 12(33), 37313 (2020)
99. S. M. Beladi-Mousavi, A. M. Pourrahimi, Z. Sofer, and M. Pumera, Atomically thin 2D-arsenene by liquid-phased exfoliation: Toward selective vapor sensing, *Adv. Funct. Mater.* 29(5), 1807004 (2019)
100. C. Zhang, M. Liang, S. H. Park, Z. Lin, A. Seral-Ascaso, L. Wang, A. Pakdel, C. Ó. Coileáin, J. Boland, O. Ronan, N. McEvoy, B. Lu, Y. Wang, Y. Xia, J. N. Coleman, and V. Nicolosi, Extra lithium-ion storage capacity enabled by liquid-phase exfoliated indium selenide nanosheets conductive network, *Energy Environ. Sci.* 13(7), 2124 (2020)
101. M. Bat-Erdene, M. Batmunkh, C. J. Shearer, S. A. Tawfik, M. J. Ford, L. Yu, A. J. Sibley, A. D. Slattery, J. S. Quinton, C. T. Gibson, and J. G. Shapter, Efficient and fast synthesis of few-layer black phosphorus via microwave-assisted liquid-phase exfoliation, *Small Methods* 1(12), 1700260 (2017)
102. Z. J. Xie, C. Y. Xing, W. C. Huang, T. J. Fan, Z. J. Li, J. L. Zhao, Y. J. Xiang, Z. N. Guo, J. Q. Li, Z. G. Yang, B. Q. Dong, J. L. Qu, D. Y. Fan, and H. Zhang, Ultrathin 2D nonlayered tellurium nanosheets: Facile liquid-phase exfoliation, characterization, and photoresponse with high performance and enhanced stability, *Adv. Funct. Mater.* 28(16), 1705833 (2018)
103. X. Li, L. Colombo, and R. S. Ruoff, Synthesis of graphene films on copper foils by chemical vapor deposition, *Adv. Mater.* 28(29), 6247 (2016)
104. Y. Huang, K. Yu, H. Li, K. Xu, Z. Liang, D. Walker, P. Ferreira, P. Fischer, and D. Fan, Scalable fabrication of molybdenum disulfide nanostructures and their assembly, *Adv. Mater.* 32(43), 2003439 (2020)
105. X. B. Li, X. Wang, J. H. Hong, D. Y. Liu, Q. L. Feng, Z. B. Lei, K. H. Liu, F. Ding, and H. Xu, Nanoassembly growth model for subdomain and grain boundary formation in 1T′ layered ReS_2, *Adv. Funct. Mater.* 29(49), 1906385 (2019)

106. B. Q. Huang, Z. H. Lei, X. H. Cao, A. X. Wei, L. L. Tao, Y. B. Yang, J. Liu, Z. Q. Zheng, and Y. Zhao, High-quality two-dimensional tellurium flakes grown by high-temperature vapor deposition, *J. Mater. Chem. C* 9(40), 14394 (2021)
107. X. Zhang, J. Z. Jiang, A. A. Suleiman, B. Jin, X. Z. Hu, X. Zhou, and T. Y. Zhai, Hydrogen-assisted growth of ultrathin Te flakes with giant gate-dependent photoresponse, *Adv. Funct. Mater.* 29(49), 1906585 (2019)
108. M. Tanaka, M. Auffray, H. Nakanotani, and C. Adachi, Spontaneous formation of metastable orientation with well-organized permanent dipole moment in organic glassy films, *Nat. Mater.* 21(7), 819 (2022)
109. D. Higgins, A. T. Landers, Y. Ji, S. Nitopi, C. G. Morales-Guio, L. Wang, K. Chan, C. Hahn, and T. F. Jaramillo, Guiding electrochemical carbon dioxide reduction toward carbonyls using Copper silver thin films with interphase miscibility, *ACS Energy Lett.* 3(12), 2947 (2018)
110. Y. Wang, L. Gan, J. Chen, R. Yang, and T. Zhai, Achieving highly uniform two-dimensional PbI_2 flakes for photodetectors via space confined physical vapor deposition, *Sci. Bull. (Beijing)* 62(24), 1654 (2017)
111. A. Apte, E. Bianco, A. Krishnamoorthy, S. Yazdi, R. Rao, N. Glavin, H. Kumazoe, V. Varshney, A. Roy, F. Shimojo, E. Ringe, R. K. Kalia, A. Nakano, C. S. Tiwari, P. Vashishta, V. Kochat and P. M. Ajayan, Polytypism in ultrathin tellurium, *2D Mater.* 6(1), 015013 (2019)
112. C. S. Zhao, H. Batiz, B. Yasar, H. Kim, W. B. Ji, M. C. Scott, D. C. Chrzan, and A. Javey, Tellurium single-crystal arrays by low-temperature evaporation and crystallization, *Adv. Mater.* 33(37), 2100860 (2021)
113. J. T. Lu, L. J. Zhang, C. R. Ma, W. J. Huang, Q. J. Ye, H. X. Yi, Z. Q. Zheng, G. W. Yang, C. A. Liu, and J. D. Yao, In situ integration of Te/Si 2D/3D heterojunction photodetectors toward UV-Vis-IR ultra-broadband photoelectric technologies, *Nanoscale* 14(16), 6228 (2022)
114. Q. S. Wang, M. Safdar, K. Xu, M. Mirza, Z. X. Wang, and J. He, Van der Waals epitaxy and photoresponse of hexagonal tellurium nanoplates on flexible mica sheets, *ACS Nano* 8(7), 7497 (2014)
115. I. Ferain, C. A. Colinge, and J. P. Colinge, Multigate transistors as the future of classical metal–oxide–semiconductor field-effect transistors, *Nature* 479(7373), 310 (2011)
116. M. M. Waldrop, The chips are down for Moore's law, *Nature* 530(7589), 144 (2016)
117. P. Yang, J. J. Zha, G. Y. Gao, L. Zheng, H. X. Huang, Y. P. Xia, S. C. Xu, T. F. Xiong, Z. M. Zhang, Z. B. Yang, Y. Chen, D. K. Ki, J. J. Liou, W. G. Liao, and C. L. Tan, Growth of tellurium nanobelts on h-BN for p-type transistors with ultrahigh hole mobility, *Nano-Micro Lett.* 14(1), 109 (2022)
118. J. K. Qin, P. Y. Liao, M. Si, S. Gao, G. Qiu, J. Jian, Q. Wang, S. Q. Zhang, S. Huang, A. Charnas, Y. Wang, M. J. Kim, W. Wu, X. Xu, H. Y. Wang, L. Yang, Y. Khin Yap, and P. D. Ye, Raman response and transport properties of tellurium atomic chains encapsulated in nanotubes, *Nat. Electron.* 3(3), 141 (2020)
119. T. Kim, C. H. Choi, P. Byeon, M. Lee, A. Song, K. B. Chung, S. Han, S. Y. Chung, K. S. Park, and J. K. Jeong, Growth of high-quality semiconducting tellurium films for high-performance p-channel field-effect transistors with wafer-scale uniformity, *npj 2D Mater. Appl.* 6(1), 4 (2022)
120. Y. Liu, J. Guo, E. B. Zhu, L. Liao, S. J. Lee, M. N. Ding, I. Shakir, V. Gambin, Y. Huang, and X. F. Duan, Approaching the schottky-mott limit in van der waals metal-semiconductor junctions, *Nature* 557(7707), 696 (2018)
121. S. Song, Y. Sim, S. Y. Kim, J. H. Kim, I. Oh, W. Na, D. H. Lee, J. Wang, S. Yan, Y. Liu, J. Kwak, J. H. Chen, H. Cheong, J. W. Yoo, Z. Lee, and S. Y. Kwon, Wafer-scale production of patterned transition metal ditelluride layers for two-dimensional metal-semiconductor contacts at the Schottky–Mott limit, *Nat. Electron.* 3(4), 207 (2020)
122. P. C. Shen, C. Su, Y. X. Lin, A. S. Chou, C. C. Cheng, J. H. Park, M. H. Chiu, A. Y. Lu, H. L. Tang, M. M. Tavakoli, G. Pitner, X. Ji, Z. Y. Cai, N. N. Mao, J. T. Wang, V. C. Tung, J. Li, J. Bokor, A. Zettl, C. I. Wu, T. Palacios, L. J. Li, and J. Kong, Ultralow contact resistance between semimetal and monolayer semiconductors, *Nature* 593(7858), 211 (2021)
123. M. Wu, Y. Xiao, Y. Zeng, Y. Zhou, X. Zeng, L. Zhang, and W. Liao, Synthesis of two-dimensional transition metal dichalcogenides for electronics and optoelectronics, *InfoMat* 3(4), 362 (2021)
124. X. K. Zhang, Z. Kang, L. Gao, B. S. Liu, H. H. Yu, Q. L. Liao, Z. Zhang, and Y. Zhang, Molecule-upgraded van der waals contacts for Schottky-barrier-free electronics, *Adv. Mater.* 33(45), 2104935 (2021)
125. Y. Y. Liu, P. Stradins, and S. H. Wei, Van der Waals metal-semiconductor junction: Weak Fermi level pinning enables effective tuning of Schottky barrier, *Sci. Adv.* 2(4), e1600069 (2016)
126. Y. Wang, H. Yuan, Z. Li, and J. Yang, Schottky and ohmic contacts at α-tellurene/2D metal interfaces, *ACS Appl. Electron. Mater.* 4(3), 1082 (2022)
127. X. K. Zhang, H. H. Yu, W. H. Tang, X. F. Wei, L. Gao, M. Y. Hong, Q. L. Liao, Z. Kang, Z. Zhang, and Y. Zhang, All-van-der-Waals barrier-free contacts for high-mobility transistors, *Adv. Mater.* 34(34), 2202345 (2022)
128. W. Jiang, X. D. Wang, Y. Chen, S. Q. Wu, B. M. Wu, X. Yang, T. Lin, H. Shen, X. J. Meng, X. Wu, J. H. Chu, and J. L. Wang, End-bonded contacts of tellurium transistors, *ACS Appl. Mater. Interfaces* 13(6), 7766 (2021)
129. D. A. Nguyen, D. Y. Park, J. Lee, N. T. Duong, C. Park, D. H. Nguyen, T. S. Le, D. Suh, H. Yang, and M. S. Jeong, Patterning of type-II Dirac semimetal $PtTe_2$ for optimized interface of tellurene optoelectronic device, *Nano Energy* 86, 106049 (2021)
130. W. L. Ma, Y. Q. Gao, L. Y. Shang, W. Zhou, N. J. Yao, L. Jiang, Q. X. Qiu, J. B. Li, Y. Shi, Z. G. Hu, and Z. M. Huang, Ultrabroadband tellurium photoelectric detector from visible to millimeter wave, *Adv. Sci.*

(Weinh.) 9(5), 2103873 (2022)

131. S. Q. Lin, W. Li, Z. W. Chen, J. W. Shen, B. H. Ge, and Y. Z. Pei, Tellurium as a high-performance elemental thermoelectric, *Nat. Commun.* 7(1), 10287 (2016)
132. G. Qiu, S. Huang, M. Segovia, P. K. Venuthurumilli, Y. Wang, W. Wu, X. Xu, and P. D. Ye, Thermoelectric performance of 2D tellurium with accumulation contacts, *Nano Lett.* 19(3), 1955 (2019)
133. Z. P. Sun, A. Martinez, and F. Wang, Optical modulators with 2D layered materials, *Nat. Photonics* 10(4), 227 (2016)
134. S. Deckoff-Jones, Y. X. Wang, H. T. Lin, W. Z. Wu, and J. J. Hu, Tellurene: A multifunctional material for midinfrared optoelectronics, *ACS Photonics* 6(7), 1632 (2019)
135. H. T. Lin, Y. Song, Y. Z. Huang, D. Kita, S. Deckoff-Jones, K. Q. Wang, L. Li, J. Y. Li, H. Y. Zheng, Z. Q. Luo, H. Z. Wang, S. Novak, A. Yadav, C. C. Huang, R. J. Shiue, D. Englund, T. Gu, D. Hewak, K. Richardson, J. Kong, and J. J. Hu, Chalcogenide glass-on-graphene photonics, *Nat. Photonics* 11(12), 798 (2017)
136. Z. Ma, K. Kikunaga, H. Wang, S. Sun, R. Amin, R. Maiti, M. H. Tahersima, H. Dalir, M. Miscuglio, and V. J. Sorger, Compact graphene plasmonic slot photodetector on silicon-on-insulator with high responsivity, *ACS Photonics* 7(4), 932 (2020)
137. H. Y. Lan, Y. H. Hsieh, Z. Y. Chiao, D. Jariwala, M. H. Shih, T. J. Yen, O. Hess, and Y. J. Lu, Gate-tunable plasmon-enhanced photodetection in a monolayer MoS_2 phototransistor with ultrahigh photoresponsivity, *Nano Lett.* 21(7), 3083 (2021)
138. S. Castilla, I. Vangelidis, V. V. Pusapati, J. Goldstein, M. Autore, T. Slipchenko, K. Rajendran, S. Kim, K. Watanabe, T. Taniguchi, L. Martin-Moreno, D. Englund, K. J. Tielrooij, R. Hillenbrand, E. Lidorikis, and F. H. L. Koppens, Plasmonic antenna coupling to hyperbolic phonon-polaritons for sensitive and fast mid-infrared photodetection with graphene, *Nat. Commun.* 11(1), 4872 (2020)
139. Y. Zhang, F. Zhang, L. M. Wu, Y. P. Zhang, W. C. Huang, Y. F. Tang, L. P. Hu, P. Huang, X. W. Zhang, and H. Zhang, Van der Waals integration of bismuth quantum dots-decorated tellurium nanotubes (Te@Bi) heterojunctions and plasma-enhanced optoelectronic applications, *Small* 15(47), 1903233 (2019)
140. Q. Zhao, F. Gao, H. Chen, W. Gao, M. Xia, Y. Pan, H. Shi, S. Su, X. Fang, and J. Li, High performance polarization-sensitive self-powered imaging photodetectors based on a p-Te/n-$MoSe_2$ van der Waals heterojunction with strong interlayer transition, *Mater. Horiz.* 8(11), 3113 (2021)
141. J. Yao, F. Chen, J. Li, J. Du, D. Wu, Y. Tian, C. Zhang, J. Yang, X. Li, and P. Lin, A high-performance short-wave infrared phototransistor based on a 2D tellurium/MoS_2 van der Waals heterojunction, *J. Mater. Chem. C* 9(38), 13123 (2021)
142. M. Peng, Y. Y. Yu, Z. Wang, X. Fu, Y. Gu, Y. Wang, K. Zhang, Z. H. Zhang, M. Huang, Z. Z. Cui, F. Zhong, P. S. Wu, J. F. Ye, T. F. Xu, Q. Li, P. Wang, F. Y. Yue, F. Wu, J. N. Dai, C. Q. Chen, and W. D. Hu, Room-temperature blackbody-sensitive and fast infrared photodetectors based on 2D tellurium/graphene van der Waals heterojunction, *ACS Photonics* 9(5), 1775 (2022)
143. Y. Liu, N. O. Weiss, X. D. Duan, H. C. Cheng, Y. Huang, and X. F. Duan, Van der Waals heterostructures and devices, *Nat. Rev. Mater.* 1(9), 16042 (2016)
144. H. Y. Lee and S. Kim, Nanowires for 2D material-based photonic and optoelectronic devices, *Nanophotonics* 11(11), 2571 (2022)
145. J. Z. Wu and M. Gong, Nanohybrid photodetectors, *Adv. Photon. Res.* 2(7), 2100015 (2021)
146. T. Zheng, M. Yang, Y. Sun, L. Han, Y. Pan, Q. Zhao, Z. Zheng, N. Huo, W. Gao, and J. Li, A solution-fabricated tellurium/silicon mixed-dimensional van der Waals heterojunction for self-powered photodetectors, *J. Mater. Chem. C* 10(18), 7283 (2022)
147. X. Cao, Z. Lei, B. Huang, A. Wei, L. Tao, Y. Yang, Z. Zheng, X. Feng, J. Li, and Y. Zhao, Non-layered Te/In_2S_3 tunneling heterojunctions with ultrahigh photoresponsivity and fast photoresponse, *Small* 18(18), 2200445 (2022)
148. L. Han, M. Yang, P. Wen, W. Gao, N. Huo, and J. Li, A high performance self-powered photodetector based on a 1D Te-2D WS_2 mixed-dimensional heterostructure, *Nanoscale Adv.* 3(9), 2657 (2021)
149. J. J. Tao, J. Jiang, S. N. Zhao, Y. Zhang, X. X. Li, X. Fang, P. Wang, W. Hu, Y. H. Lee, H. L. Lu, and D. W. Zhang, Fabrication of 1D Te/2D ReS_2 mixed-dimensional van der Waals p–n heterojunction for high-performance phototransistor, *ACS Nano* 15(2), 3241 (2021)
150. W. Wang, Y. Meng, W. Wang, Z. Zhang, P. Xie, Z. Lai, X. Bu, Y. Li, C. Liu, Z. Yang, S. Yip, and J. C. Ho, Highly efficient full van der Waals 1D p-Te/2D n-Bi_2O_2Se heterodiodes with nanoscale ultra-photosensitive channels, *Adv. Funct. Mater.* 32(30), 2203003 (2022)
151. D. Zhao, Y. Chen, W. Jiang, X. Wang, J. Liu, X. Huang, S. Han, T. Lin, H. Shen, X. Wang, W. Hu, X. Meng, J. Chu, and J. Wang, Gate-tunable photodiodes based on mixed-dimensional Te/$MoTe_2$ van der Waals heterojunctions, *Adv. Electron. Mater.* 7(5), 2001066 (2021)
152. X. Zhang, Y. Yang, Z. Li, X. Liu, C. Zhang, S. Peng, J. Han, H. Zhou, J. Gou, F. Xiu, and J. Wang, Weyl semiconductor Te/Sb_2Se_3 heterostructure for broadband photodetection and its binary photoresponse by C_{60} as charge-regulation medium, *Adv. Opt. Mater.* 9(21), 2101256 (2021)
153. M. Naqi, K. H. Choi, Y. Cho, H. Y. Rho, H. Cho, P. Pujar, N. liu, H. S. Kim, J. Y. Choi, and S. Kim, Flexible platform oriented: Unipolar-type hybrid dual-channel scalable field-effect phototransistors array based on tellurium nanowires and tellurium-film with highly linear photoresponsivity, *Adv. Electron. Mater.* 8(7), 2101331 (2022)